

Engineering Three-Dimensional (3D) Out-of-Plane Graphene Edge Sites for Highly-Selective Two-Electron Oxygen Reduction Electrocatalysis

San Roman, D.,^{1^} Krishnamurthy, D.,^{2^} Garg, R.,¹ Nuhfer, N.,¹ Viswanathan, V.,^{2} Cohen-Karni, T.^{1,3,*}*

¹ *Department of Material Science and Engineering, Carnegie Mellon University, Pittsburgh, Pennsylvania, 15213, USA.*

² *Department of Mechanical Engineering, Carnegie Mellon University, Pittsburgh, Pennsylvania, 15213, USA.*

³ *Department of Biomedical Engineering, Carnegie Mellon University, Pittsburgh, Pennsylvania, 15213, USA.*

[^] *Equal Contribution*

^{*} *Corresponding author*

Abstract

Selective two-electron oxygen reduction reaction (ORR) offers a promising route for hydrogen peroxide synthesis. Defective sp^2 carbon-based materials are attractive, low-cost electrocatalysts for this process. However, due to a wide-range of possible defect structures formed during material synthesis, identification and fabrication of precise active sites remain a challenge. Here, we report a highly-tunable graphene-based electrocatalyst, nanowire-templated three-dimensional fuzzy graphene (NT-3DFG), with excellent efficiency (~ 30 mV onset potential) and selectivity (93 ± 3 % H_2O_2) for two-electron ORR after process optimization for high densities of graphene edges. Using surface characterization and density functional theory calculations, we find that the edge sites are saturated by carbonyl (C=O) or hydrogen (C-H) groups, and that the zigzag edge sites with high coverage of carbonyl groups could lead to selective, two-electron ORR. We derive a general geometric descriptor based on the local coordination environment that provides activity predictions of graphene surface sites with ~ 0.1 V accuracy. Our combined synthesis and model-based approach accelerates active site characterization and carbon-based electrocatalyst discovery.

Introduction

Hydrogen peroxide (H_2O_2) is a versatile and environmentally compatible oxidizing agent, and the relative safety and simplicity of its use has led a number of applications in paper and textile manufacturing and wastewater treatment systems.¹ Currently, H_2O_2 is produced through an energy-intensive anthraquinone oxidation process that requires large-scale infrastructure and generates considerable amounts of waste.¹ On-site electrochemical production where oxygen reduction reactions (ORR) directly yield H_2O_2 offers an attractive, alternative synthesis route,^{2, 3} and recent interest in the sustainable electrochemical production of H_2O_2 has sparked a search for low-cost and selective electrocatalysts.⁴⁻⁸ Noble metal alloys, such as Pd–Au and Pt–Hg, can exhibit small overpotentials for ORR and high H_2O_2 selectivity,^{4, 5} but the cost and scarcity of these materials impede their widespread adoption. Metal-free carbon-based materials (e.g., oxidized carbon nanotubes,⁶ defective carbons,⁷ and reduced graphene oxide⁸) have shown promise as selective H_2O_2 electrocatalysts. Given the complexity of carbon structures, it is generally difficult to pinpoint the exact nature of the active site or fabricate model catalysts with a specified number or type of active sites. Additionally, the state of the surface under reaction conditions may differ vastly from pristine conditions,⁹ and given equilibrium through water discharge reactions, numerous possible edge site terminations (OH^- , H^- , or O^-) may be active.¹⁰ Generating controlled catalytic sites in sp^2 -hybridized carbon structures with known defects and morphologies through careful synthesis of graphene-based materials provides an approach to systematically address this.¹¹ This decreases the phase space of active sites and allows the determination of electrocatalytic activity and selectivity using density functional theory (DFT) calculations.^{12, 13}

Here we report a novel graphene-based hybrid nanomaterial, nanowire-templated out-of-plane three-dimensional fuzzy graphene¹⁴ (NT-3DFG), and through tunable synthesis procedures, we demonstrate precise control over the size and density of out-of-plane graphene flakes and edges. By increasing the density of out-of-plane graphene edges, NT-3DFG electrodes displayed improved ORR activity (both increased current density and lowered onset potentials). NT-3DFG optimized for high densities of graphene edges showed superior performance as a H_2O_2 electrocatalyst with excellent efficiency (~30 mV onset potential) and selectivity ($93 \pm 3\%$ H_2O_2). We constructed surface Pourbaix diagrams using DFT

calculations to probe the termination groups for the graphene edge sites (both armchair and zig-zag) as a function of reaction conditions (pH and electrode potential), and our analysis suggests that both armchair and zig-zag edge sites are saturated by high coverage carbonyl (C=O) groups. We explored a range of possible active sites to account for kinetically stable sites in addition to thermodynamically stable configurations. We found that the oxygenation process significantly alters the surface energies of graphene edges and posit that zigzag graphene edges with high coverage carbonyl groups are likely sites for selective two-electron ORR. A geometric descriptor for H₂O₂ activity was derived on the basis of the active site coordination environment, which enables activity predictions of graphene surface sites with high (within ≈ 0.1 V) accuracy. Combining tunable catalyst synthesis methods with descriptive theoretical models as shown herein will continue to enable active site determination and accelerated material discovery within carbon-based two-dimensional materials and heterostructures.

Results

Controlling catalyst morphology. To better understand the contribution of graphene edges to ORR in sp² hybridized carbons, the number of out-of-plane graphene edges in catalyst electrodes was varied by controlling the synthesis temperature and time. This study leveraged a highly-tunable plasma enhanced chemical vapor deposition (PECVD) synthesis process to achieve nanowire-templated three-dimensional fuzzy graphene (NT-3DFG)¹⁴ with varying graphene flake densities and size (**Figure 1.a**). Scanning electron microscope (SEM) imaging (**Figure 1.b-d**) revealed increasing NT-3DFG flake size (686 ± 61 , 974 ± 115 , and 1147 ± 84 nm NT-3DFG diameters) and densities (429 ± 58 , 2987 ± 354 , and 3297 ± 532 μm^{-2}) for samples synthesized at 700, 900, and 1100 °C for 30 min, respectively (**Figure 1.e,f**). These observations can be attributed to increasing nucleation and growth rates of graphene flakes through PECVD.¹⁵ NT-3DFG growth follows Arrhenius kinetics with the growth activation energy (E_A) calculated as 0.16 ± 0.01 eV (**Figure S1**). The calculated activation energy is lower than literature reported activation energy for vertical graphene nanosheets ($E_A = 0.57$ eV),¹⁶ suggesting that the faster growth rate in our synthesis protocol might be responsible for increased flake size and density. NT-3DFG synthesis was also performed at 1100 °C for 60 and 120 min to further increase flake size and density.¹⁴ SEM images showed a similar surface topology at extended growth times, while the NT-3DFG diameter increased with synthesis

time to 1883 ± 214 and 4231 ± 641 nm for samples synthesized at 1100 °C for 60 and 120 min, respectively (**Figure S2**).

Across all synthesis conditions, characteristic Raman D, G, and 2D peaks for NT-3DFG were observed (**Figure 2.a,d** and **Table S1**).¹⁴ The contribution of bulk and edge defects to the D peak in the NT-3DFG across all synthesis conditions was determined by investigating the correlation between the intensity ratio of the D and G peak ($I_D I_G^{-1}$), full width half maximum of the G peak ($FWHM_G$), and the dispersion of the G peak ($Disp_G$).^{14, 17-19} The absence of clear correlations between $I_D I_G^{-1}$, $FWHM_G$, and $Disp_G$ (**Figure 2.c,f** and **Figure S3**) suggests that the primary contribution to the D peak in NT-3DFG arises from edges rather than bulk defects. All samples also exhibited a saturation of the G peak position near ~ 1600 cm^{-1} and $Disp_G < 0.10$ $cm^{-1} nm^{-1}$, which indicates the presence of sp^2 hybridization in NT-3DFG and absence of large structural defects.^{19, 20} The $FWHM_G$ increased (40.8 ± 2.2 cm^{-1} , 47.2 ± 1.6 , and 49.0 ± 1.4 cm^{-1}) as NT-3DFG synthesis temperature (700 °C, 900 °C, and 1100 °C, respectively) increased, indicating an increase in edge defect density (**Figure 2.b.I**).¹⁸ The rise in the $I_D I_G^{-1}$ (2.34 ± 0.52 to 3.59 ± 0.15) for synthesis temperatures 700 °C and 900 °C, respectively, (**Figure 2.b.II**) is attributed to the increase in edge defects in NT-3DFG that allow D peak activation.¹⁴ Upon further increase in NT-3DFG synthesis temperature, $I_D I_G^{-1}$ declined; The decline in $I_D I_G^{-1}$ was rationalized by high defect densities that limit the number of near-by aromatic carbon rings that are necessary for D peak activation.^{21, 22} For NT-3DFG, it is hypothesized the defective out-of-plane graphene edges brought in close proximity effectively screen the D peak-active regions of nearby intact sp^2 lattices. For extended NT-3DFG synthesis times (60 and 120 min) at 1100 °C, the $FWHM_G$ saturates at ~ 60 cm^{-1} (**Figure 2.e.I**), and $I_D I_G^{-1}$ decreases and saturates at ~ 2.4 (**Figure 2.e.II**), suggesting that highest edge defect densities for NT-3DFG have been achieved at these conditions.

To further clarify the nature of the graphene flakes in NT-3DFG, high-resolution transmission electron spectroscopy (HR-TEM) imaging was conducted (**Figure S4**). At low synthesis temperatures, multi-layered graphene flakes are visible at the circumferential surface of NT-3DFG, which appear similar in nature to folded turbostratic graphite.²³ At the 1100 °C synthesis temperature, many graphene flakes are visible at the circumferential surface which resemble suspended graphene sheets.²⁴

ORR activity of NT-3DFG. To assess the ORR activity of NT-3DFG across synthesis conditions, cyclic voltammetry (CV) experiments were conducted in 0.1 M KOH at a scan rate of 50 mV s⁻¹. All samples showed significant cathodic peaks under bubbled O₂ that were absent in the presence of pure N₂, indicating the reduction of O₂ at the NT-3DFG electrode (**Figure 3.a,b**). The ORR onset potential (potential measured at 0.1 mA cm⁻² after N₂ baseline current subtraction) increased by ~120 mV when the NT-3DFG synthesis temperature was increased from 700 to 900 °C with further onset potential increase (~40 mV) for samples synthesized at 900 to 1100 °C (**Figure S5.a**). The ORR cathodic peak densities, j_{pc} , were 0.23 ± 0.08, 0.27 ± 0.04, and 0.45 ± 0.05 mA cm⁻² for samples synthesized at 700, 900, and 1100 °C, respectively (**Figure S5.b**). For NT-3DFG synthesized at 1100 °C for extended synthesis times of 60 and 120 min (**Figure 3.b**), smaller increases in the onset potential, ~10 mV (**Figure S5.c**), and saturation of j_{pc} , 0.67 ± 0.04 and 0.65 ± 0.01 mA cm⁻², respectively (**Figure S5.d**), were observed. The dramatic increases in ORR activity for NT-3DFG synthesized at 700 °C versus samples synthesized at 900 °C & 1100 °C can be rationalized by the near 10-fold increase in NT3DFG edge density. These results suggest that the graphene edges in NT-3DFG are likely ORR active sites. Upon increasing NT-3DFG synthesis temperature and time, the formation of a second reduction peak occurred at lower potentials (~0.1 V vs. RHE). ORR proceeds through a 2 e⁻ pathway or 4 e⁻ pathway, and the presence of 2 peaks may indicate a two-step, 2 e⁻ process to form OH⁻ at high overpotentials.²⁵

Quantitative measurements of the reaction products were performed by chronoamperometry (CA) and iodometric titration of H₂O₂.^{8, 26} The ratio of the number of electrons transferred during ORR at 0.5 V vs. RHE (**Figure S6**) to the number of H₂O₂ molecules measured via titration was 2.16 ± 0.09 (**Table S7**). A ratio close to 2 indicates that the 2 e⁻ reduction pathway for ORR is preferred for NT-3DFG. This material showed a high H₂O₂ selectivity of 93 ± 3 % which is higher or comparable to precious metal alloy catalysts⁴ and other nanocarbon catalysts.⁶⁻⁸

NT-3DFG samples with an average mass loading of 0.41 ± 0.05 mg cm⁻² were transferred to 5 mm-diameter disks for rotating disk electrode (RDE) testing. The pronounced catalytic effect of NT-3DFG over a polished glassy carbon electrode is demonstrated in the linear sweep voltammetry (LSV) curves in **Figure 3.c**. At a scan rate of 10 mV s⁻¹ and rotational speed of 1600 rpm, the catalyst quickly achieved a high limiting current density of 2.97 ± 0.02 mA cm⁻², indicating a catalytic surface with many ORR active sites.

Based on a calculated equilibrium potential of 0.825 V versus RHE for 2 e⁻ reduction in O₂-saturated 0.1 M KOH, a half-wave overpotential of ~160 mV was measured and the onset overpotential for ORR was as low as ~30 mV. The NT-3DFG catalyst also exhibited facile current response within the kinetically-controlled regime, demonstrated by a low Tafel slope of 44 ± 2 mV dec⁻¹. The stability of NT-3DFG electrodes during ORR was investigated by 15-hour CA testing (**Figure 3.d**), and negligible change in the current output was observed. The NT-3DFG electrodes remained intact after ORR testing as evidenced by SEM (**Figure S7**) and Raman analysis (**Figure S8**). NT-3DFG's low overpotential for ORR, high reaction selectivity, and electrochemical stability demonstrate ideal catalytic behavior for H₂O₂ generation under alkaline conditions.

Surface state of NT-3DFG. NT-3DFG exhibits a valence band spectra (**Figure S9.a**) similar to that of graphene,²⁷ and shows electronic states up to the Fermi level (**Figure S9.b**), indicating a metallic or semi-metallic electronic nature.²⁸ The work function for NT-3DFG (**Figure S9.c**) was measured to be 4.6 ± 0.05 eV, which is similar to literature values for graphite (~4.6 eV) and single layer graphene (~4.5-4.7 eV).²⁹ **Figure 4.a** provides a representative X-ray photoemission spectroscopy (XPS) survey scan for NT-3DFG before and after ORR (CV and H₂O₂ selectivity testing). Elemental surveys measured 11.5 ± 0.5 at. % oxygen which indicated significant oxygen incorporation at the surface of NT-3DFG after ORR. The primary C1s feature at 284.1 ± 0.2 eV binding energy (BE) was attributed to sp² carbon, and the broad peak at 290.4 ± 0.2 eV BE was assigned to the π-π* plasmon loss feature (**Figure 4.b**).³⁰ After ORR testing, oxygen-carbon peaks were present in the C1s spectra (**Figure 4.c**) which were prescribed to C-OH, C=O, and O=C-OH bonds at binding energies of 285.7 ± 0.4, 286.8 ± 0.3, and 288.1 ± 0.4 eV, respectively (**Table S10**).^{6, 31} The amount of oxygen-carbon bonds detected in the C1s chemical state analysis was ~13 at. % which was consistent with survey compositions and suggested that the oxygen present after ORR testing was bonded with the carbon near NT-3DFG's surface. The O1s peak (**Figure 4.d**) was fit with three peaks for C-OH, C=O, and O=C-OH bonds at binding energies of 532.2 ± 0.2, 533.2 ± 0.2, and 531.1 ± 0.2 eV, respectively. The ratios of the oxygen groups in the O1s peak and C1s peak analysis suggest the hydroxyl groups followed by the carbonyl groups as the most prominent oxygen species on the surface after ORR.

DFT Calculations. XPS analysis revealed that NT-3DFG surface sites saturate with oxygen functional groups, which could significantly change the local electronic structure of active sites and thereby the ORR activity. We employed DFT calculations to identify the precise nature of active sites, which was central to

gaining a mechanistic understanding and interpreting the observed activity and pathway selectivity. The pristine state of active sites is modeled on a two-dimensional graphene sheet for both the zig-zag (ZZ) and armchair (AC) edge termination (**Figure 5.a**). While identifying potential active sites on the pristine surface can provide valuable information,^{6, 7} the state of the surface under reaction conditions must also be considered; the importance of integrating surface pourbaix diagrams in determining electrocatalytic activity and selectivity has been demonstrated elsewhere.³²⁻³⁶ In this work, we explicitly perform a self-consistent loop between identifying the most stable surface state and determining the activity (active site) by constructing surface Pourbaix diagrams on basal and edge sites. The most energetically favorable surface states of active sites as a function of pH and electrode potential are determined from several explored species coverage configurations of oxygen functional groups such as hydroxyl (C-OH) and carbonyl (C=O) groups.⁶ Consistent with prior studies, our thermodynamic analysis identifies basal sites to be inactive towards hydrogen peroxide formation.⁶ The analysis suggests that both AC and ZZ edge sites including those with hydrogen defects are saturated by carbonyl groups with coverage ≥ 0.5 monolayer (ML) under reaction conditions of pH = 13 and limiting potentials relevant (≈ 0.7 V vs. RHE) for hydrogen peroxide formation. The stable surface states are shown as a function of pH and U_{SHE} for ZZ and AC edge sites in the corresponding probabilistic Pourbaix diagrams (**Figures 5.b. and 5.c.** respectively) in which each predicted stable surface configuration is associated with a confidence value (c-value $\in [0,1]$) to quantify the degree of agreement at the chosen level of DFT fidelity. This approach provides a way to address a major challenge inherent to DFT, which is the sensitivity of determined surface phases towards the choice of exchange-correlation functional,^{37, 38} by leveraging a recently developed method that uses Bayesian error estimation techniques to compute the uncertainty associated with our predictions.³⁹ On all surface sites, we determine the activity for hydrogen peroxide production through the adsorption energetics of OOH^* . Based on this thermodynamic analysis, we find that AC sites with low ($\frac{1}{6}$ ML) coverage and ZZ sites with high ($\frac{3}{4}$ ML) coverage of carbonyl groups exhibit high (overpotential < 0.2 eV) activity (**Figure 5.d**). Although the active sites on the stronger binding leg of the volcano exhibit higher activity towards oxygen reduction to water from a thermodynamic standpoint,^{40, 41} favorable kinetics towards selective hydrogen peroxide formation is expected on the basis of agreement with experiments.^{42, 43} We rationalize the trends in surface energetics between various active sites, for example the stronger OOH^* -binding nature of pristine (H-covered) AC

edge sites relative to ZZ edge sites, based on electronegativity differences and associated Bader charges between the active site carbon atoms. In order to further understand and capture the effects of various bonding interactions around the active site on the catalytic activity, a geometric descriptor for the activity towards hydrogen peroxide is derived on the basis of the active site coordination environment, which enables activity predictions of graphene surface sites with high accuracy. We arrive at the model on the basis of maximizing the Bayesian information criterion given by $\Delta G_{\text{OOH}^*}^{\text{pred}}(\text{eV}) = 0.63 + 0.40N_{\text{OH}} + 0.45N_{\text{H}} + 1.44N_{\text{C-C}} + 1.27N_{\text{C-O}} + 1.31N_{\text{C-OH}} + 1.86N_{\text{C-H}}$ with a mean absolute error (MAE) of ≈ 0.1 eV, where N_{OH} and N_{H} represent the presence of OH and H functional groups adjacent to the active site carbon of interest respectively. $N_{\text{C-C}}$, $N_{\text{C-O}}$, $N_{\text{C-OH}}$ and $N_{\text{C-H}}$ represent the counts of adjacent sp^2 hybridized carbon atoms with all (three) carbon neighbors, all carbon neighbors except one -O, all carbon neighbors except one -OH, and all carbon neighbors except one -H, respectively (**Figure 5.f**). The relative magnitudes of coefficients in the model emerge to be in agreement with what is expected in terms of the weakening of OOH^* -binding caused by the presence of each kind of moiety adjacent to the active site carbon, for instance the largest weakening is expected to result from an adjacent carbon with all carbon neighbors. The geometric descriptor unifies AC and ZZ edge configurations and allows us to predict the landscape of surface energetics on graphene surfaces reasonably accurately, in addition to enabling inversion of the design problem to identify the nature of optimal active sites to be engineered for desired adsorption characteristics. Our analysis reveals that highly active sites exhibit optimal local coordination of one or two adjacent carbons that are saturated by oxygen terminations, which provides directions for rational material design within a broad range of carbon-based two-dimensional materials and heterostructures.

Discussion

Our experimental and computational findings suggest that NT-3DFG active sites are composed of both functionalized AC and ZZ edges. This is based on the computed overpotentials (within ≈ 0.1 V) of active sites for $\frac{3}{4}\text{O}^*\frac{1}{4}\text{H}^*$ ZZ, $\frac{1}{6}\text{O}^*\frac{5}{6}\text{H}^*$ AC, and $\frac{1}{2}\text{OH}^*\frac{1}{2}\text{H}^*$ AC configurations with similar coverages to the stable phases from the Pourbaix diagram. The presence of both edge types is consistent with previously proposed diffusion-limited aggregation growth models for NT-3DFG that indicate the formation of disordered edges with many possible edge states present.¹⁴ Moreover, theoretical calculations indicate that a distribution of

edge states is plausible due to small differences in formation energies with AC edges being more energetically favorable (0.2 eV per hydrogenated edge).⁴⁵

A significant presence of armchair edges based on the hydroxyl XPS signature (relative to carbonyl) is consistent with the predicted stability of OH* functionalized AC edges from the surface Pourbaix diagram. Moreover, under the reaction conditions, the theoretical analysis suggests that thermodynamically stable surface configuration is $\frac{2}{3}\text{OH}^*\frac{1}{3}\text{H}^*$ with a small fraction of functionals indicating $\frac{2}{3}\text{O}^*\frac{1}{3}\text{H}^*$ as the stable state. Similarly, the theory analysis suggests that both AC and ZZ are O* saturated sites and we attribute the reported O* XPS signature to a combination of edge site types.

The observed ORR activity of NT-3DFG could also result from kinetically stabilized edge site configurations that are predicted to exhibit high activity, although further kinetic studies are necessary to provide more insight. Our analysis suggests ways to engineer ORR active sites of edge-oriented graphene electrocatalysts through electrochemical pretreatment to generate specific edge configurations. One promising route could involve approaches that enable kinetic locking of highly active sites that may not thermodynamically stable from the Pourbaix diagram (e.g. $\frac{3}{4}\text{O}^*$). In addition, approaches to maximize the density of other potential edge configurations (e.g., mixed edges, edges at plane corners, and step edges) could lead to high activity, although additional insight from a subsequent exploration of the proposed configurations is necessary.

In summary, we report a novel graphene-based nanomaterial and controlled synthesis procedure that aids in understanding the origin of high selectivity and activity for two-electron ORR in sp^2 -hybridized carbon structures. The significance of graphene edges sites towards two-electron ORR is demonstrated by the correlation of NT-3DFG edge density and ORR activity. NT-3DFG exhibits superior performance with a hydrogen peroxide selectivity of $93 \pm 3\%$ and onset potential of ~ 30 mV. We considered also the energetically-favorable surface configuration of the graphene edges in our catalyst under alkaline conditions and found one fourth coverage by carbonyl groups (C=O) and full coverage by hydrogens (C-H) at graphene AC and ZZ edge sites, respectively. Carbonyl-covered AC and ZZ edge sites were found to exhibit the lowest overpotential towards two-electron ORR. Our findings and proposed model provide a

mechanistic understanding of two-electron ORR on graphene-based structures and offer directions for future carbon-based electrocatalyst design.

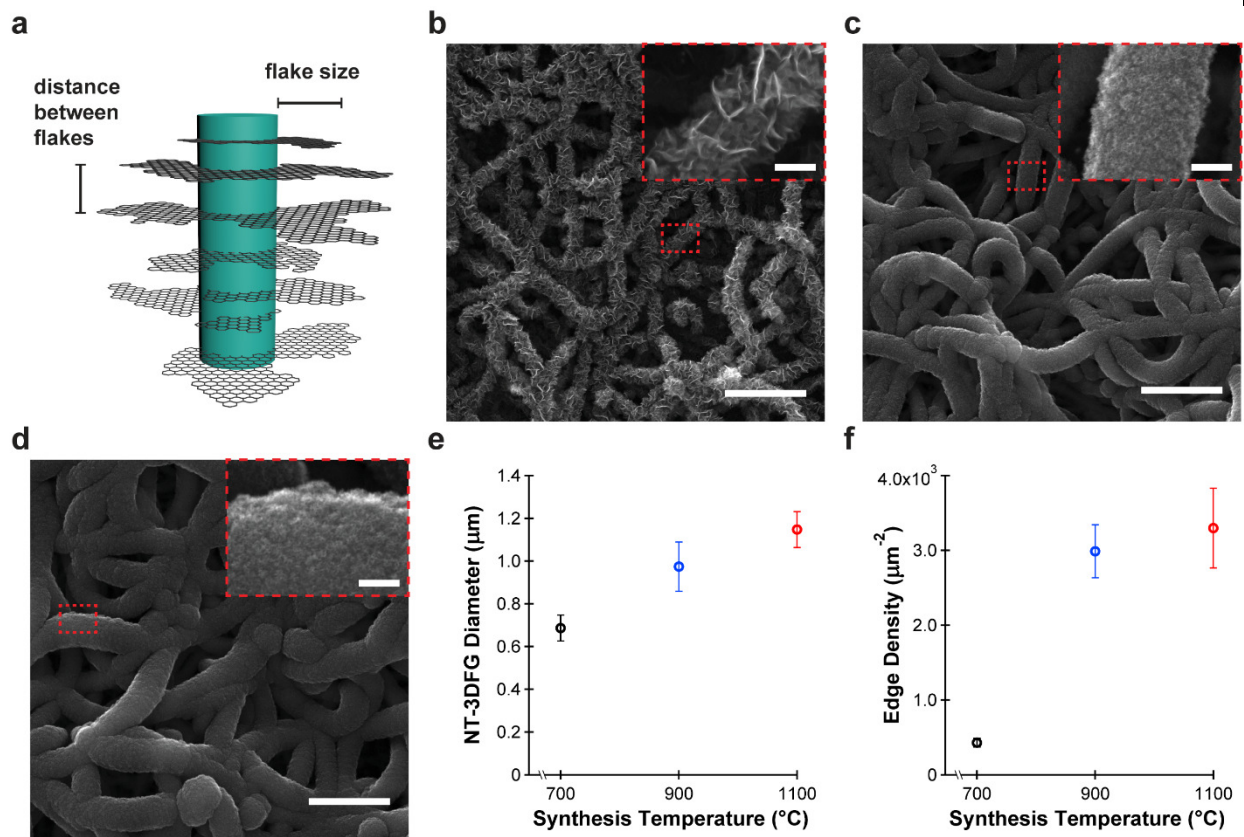
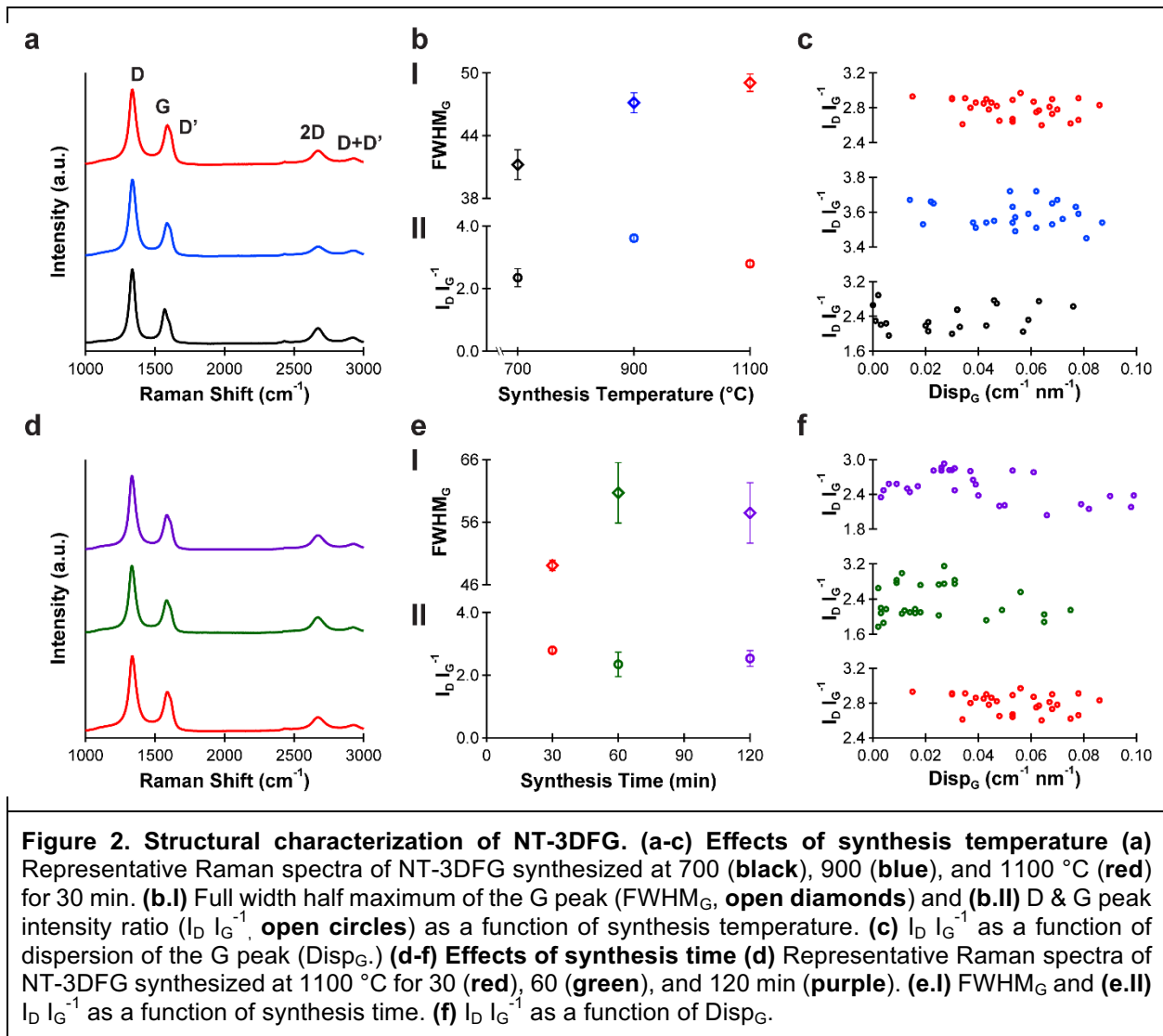


Figure 1. NT-3DFG flake size and edge density tunability. (a) Schematic representing NT-3DFG flakes. (b-d) Representative SEM images of NT-3DFG synthesized for 30 minutes at 700, 900, and 1100 °C, respectively. Scale bars: 3 μm. Insets represented by red dashed boxes show out-of-plane graphene on SiNW. Inset scale bars: 300 nm (e) NT-3DFG diameter and (f) edge density as a function of synthesis temperature.



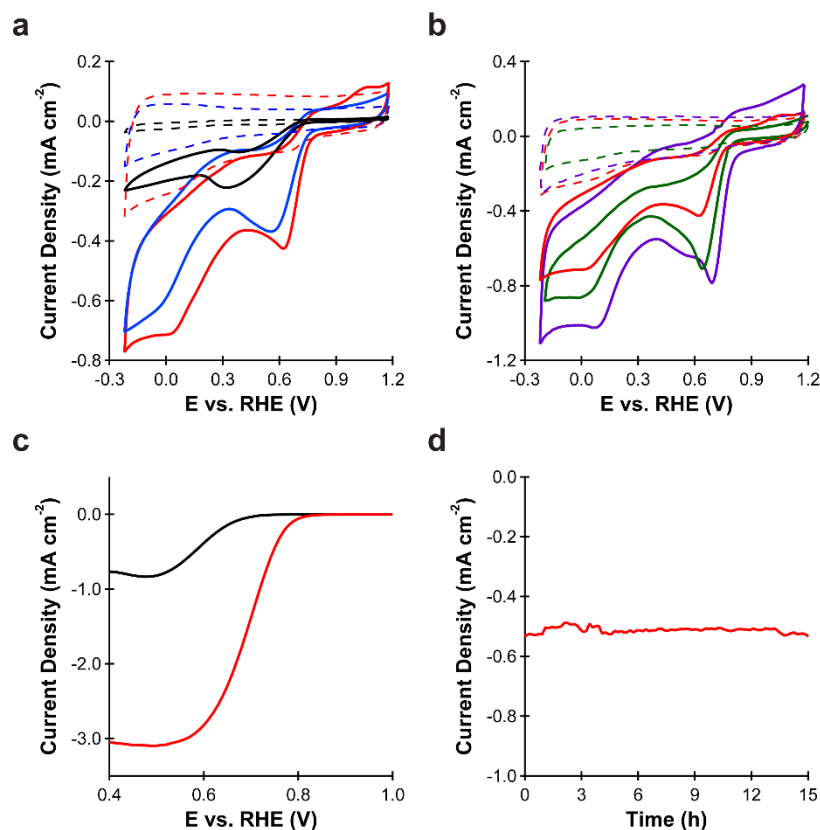
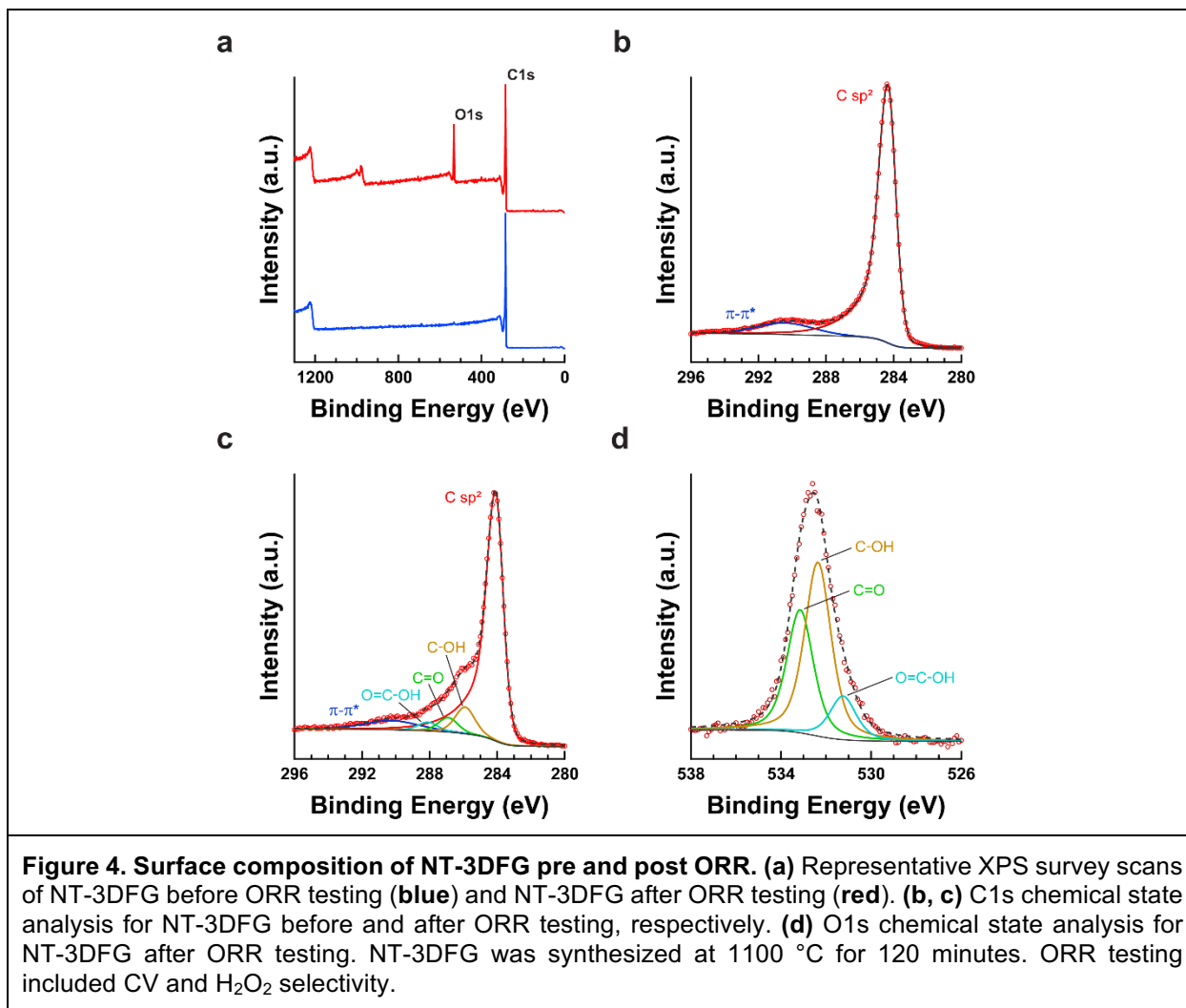


Figure 3. Oxygen reduction reactions (ORR) with NT-3DFG. (a) Representative cyclic voltammetry (CV) curves ($n = 3$) for NT-3DFG synthesized for 30 minutes at 700 (black), 900 (blue), and 1100 °C (red). (b) Representative CV curves ($n = 3$) of NT-3DFG synthesized at 1100 °C for 30 (red), 60 (green), and 120 (purple) minutes. (a, b) CV was conducted in 0.1 M KOH while bubbling N₂ (dash) & O₂ (solid) at a scan rate of 50 mV s⁻¹. (c) Representative RDE linear sweep voltammetry curves ($n = 3$) for glassy carbon electrode (black) and NT-3DFG (red) electrode synthesized at 1100 °C for 120 minutes. RDE ORR testing was conducted in 0.1 M KOH while bubbling O₂ at a scan rate of 10 mV s⁻¹ and a rotational speed of 1600 rpm. (d) Stable ORR current from NT-3DFG electrode held at 0.5 V vs. RHE while bubbling O₂ for 15 hours.



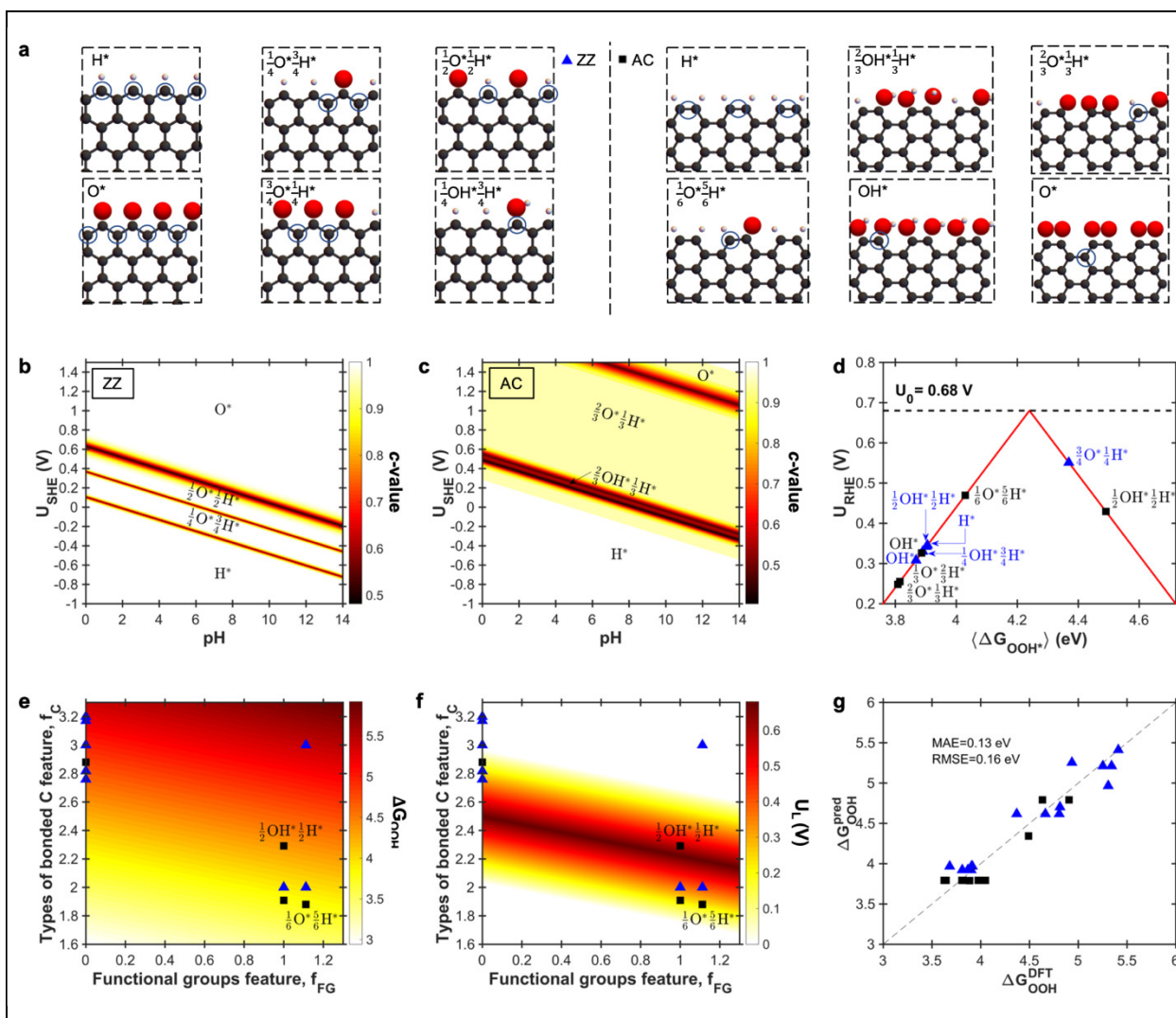


Figure 5. DFT modeling for active site determination and inverse design through a geometric activity descriptor. (a) Representative set of termination configurations of zigzag (ZZ) and armchair (AC) edge configurations with circled atoms showing the determined most stable active site for hydrogen peroxide formation. (b, c) Pourbaix diagrams showing the most energetically favorable surface species configurations for ZZ and AC edge configurations respectively, as a function of reaction conditions of electrode potential and pH. The color bar indicates the associated confidence value (c-value) with the predicted surface state, which quantifies the degree of agreement between exchange correlation functionals at the chosen level of DFT complexity. (d) Theoretical activity volcano for 2-electron oxygen reduction showing the activity predictions of various surface states. (e) Free energy of the OOH^* intermediate, ΔG_{OOH} , as a function of the local (nearest neighbor) coordination environment around the carbon active site, calculated from the proposed geometric free energy descriptor that unifies ZZ and AC edge sites. (f) Predicted activity (limiting potential) towards hydrogen peroxide formation as a function of the local environment of possible active sites. (g) Parity plot showing the effectiveness of the constructed geometric descriptor for activity over a wide (≈ 2.5 eV) descriptor range.

Methods

Nanowire Template Synthesis. Gold nanoparticle (AuNP)-catalyzed vapor-liquid-solid (VLS) growth was used to synthesize Silicon nanowires (SiNWs), following previously described synthesis.^{14, 46} In short, a 1.5 cm × 2.0 cm (100) Si substrate with a 600 nm wet thermal oxide layer (Nova Electronic Materials) or a 1.5 cm × 1.5 cm fused silica substrate (University Wafer, used for electrochemical measurements) was cleaned with acetone in an ultrasonic bath for 5 min, washed with IPA, and N₂ blow-dried. The substrate was placed in a UV–ozone system (PSD Pro series digital UV-Ozone, Novascan) for 10 min at 150 °C. The substrate was then functionalized with 450 μL (400 μL for 1.5 cm × 1.5 cm substrate) of 4:1 deionized (DI) water/poly-L-lysine (0.1% w/v, Sigma-Aldrich, Catalog No. P8920) for 8 min. Following this step, the substrate was gently washed three times in DI water and gently N₂ blow-dried. 450 μL (400 μL for 1.5 cm × 1.5 cm substrate) of 4:1 DI water/30 nm AuNP solution (Ted Pella, Inc., Catalog No. 15706-1) was dispersed onto the PLL-coated substrate for 8 min. The substrate was gently washed three times in DI water, gently N₂ blow-dried, and introduced into a custom-built CVD setup. After a baseline pressure of 1*10⁻⁵ Torr was attained, the temperature was ramped up to 450 °C in 8 min and the system was allowed to stabilize at 450 °C for 5 min. Nucleation was then conducted at 450 °C for 15 min under 80 standard cubic centimeters per minute (sccm) H₂ (Matheson Gas) and 20 sccm SiH₄ (10% in H₂, Matheson Gas) at 40 Torr. SiNW growth was then conducted at 450 °C for 100 min under 60 sccm H₂, 20 sccm SiH₄, and 20 sccm PH₃ (1000 ppm in H₂, Matheson Gas) at 40 Torr. The sample was then cooled to room temperature at base pressure.

Mesh Formation. To form SiNWs mesh, the SiNWs were collapsed by flowing liquid N₂ into the CVD quartz tube at room temperature under 200 sccm Ar flow. Then the system was evacuated to base pressure and the SiNWs mesh was annealed at 800 °C for 10 min under 200 sccm H₂ flow at 1.6 Torr. The sample was then cooled to room temperature at baseline pressure.

Out-of-Plane 3D Fuzzy Graphene Synthesis. A PECVD process was used to synthesize 3DFG on SiNWs mesh template. A SiNWs mesh was introduced into a custom-built PECVD system. The sample was centered in the tube on a carrier wafer that was 4.0 cm from the edge of the RF coil and outside the furnace. The furnace temperature was ramped up to the synthesis temperature of 700, 900, and 1100 °C in 13, 18, and 25 min, respectively, under 100 sccm Ar flow at 0.5 Torr. The system was then stabilized for

5 min under 100 sccm Ar (Matheson Gas) flow at 0.5 Torr. 3DFG synthesis was carried out at the synthesis temperature for varying synthesis time periods (30, 60, and 120 min) under 25 mTorr of CH₄ (5% CH₄ in Ar, Airgas) at 0.5 Torr. Inductively coupled plasma was generated 10 seconds before the start of the synthesis step using a 13.56 MHz RF power supply (AG 0313 Generator and AIT-600 RF, power supply and auto tuner, respectively, T&C Power Conversion, Inc.). The plasma power was held at 50 W. The furnace was moved over the sample following plasma ignition. The plasma was shut off after each synthesis step and the sample was rapidly cooled to 100 °C under 100 sccm Ar before removal from the CVD system. Three independently synthesized samples were synthesized for each PECVD synthesis condition.

Scanning Electron Microscopy (SEM) Imaging. SEM imaging was conducted using a FEI Quanta 600 field emission gun SEM. Micrographs were acquired at 20 kV accelerating voltage with a 5 mm working distance. NT-3DFG diameter was measured from high-resolution (2048 × 1768 pixels) SEM micrographs in ImageJ for 90 nanowires, across three independently synthesized samples, for each synthesis condition. The 3DFG growth rate, k , was approximated by the change in radius of the nanowire before and after synthesis with the following equation:

$$k = \frac{1}{2} \left(\frac{d_{NT-3DFG} - d_{SiNW}}{t} \right)$$

where $d_{NT-3DFG}$ is the NT-3DFG diameter, d_{SiNW} is the diameter of the nanowire template, and t is the synthesis time. The 3DFG growth rates across synthesis conditions were used to calculate the activation energy for 3DFG formation using the Arrhenius equation⁴⁷:

$$k = k_0 \times \exp \left(-\frac{E_A}{RT} \right)$$

where the activation energy (E_A) for synthesis represents the minimum energy required for growth of the out-of-plane graphene flake structures of NT-3DFG. Edge density analysis was performed to determine NT-3DFG flake edges along individual nanowires using Matlab and a Canny edge detection protocol with least count and edge connections.⁴⁸ Representative SEM images with their corresponding edge density maps are shown in **Figure S10**. Using an Au/C calibration specimen (High Resolution Gold on Carbon, TedPella, Catalog No. 617) and measuring the pitch of 30 line scans across Au nanoparticles, the SEM resolution was determined to be 5 nm. Edge features below the resolution limit were excluded from edge

analysis. Edge density measurements were performed on high-resolution SEM images corresponding to 30 nanowires, across three independently synthesized samples, representing NT-3DFG synthesized at 700, 900, and 1100 °C for 30 min.

Transmission Electron Microscopy (TEM) Imaging. TEM imaging was conducted using a FEI Titan G2 80–300 Cs-corrected TEM/STEM fitted with a high resolution Gatan Imaging Filter Tridiem energy-filter. High-resolution TEM (HRTEM) images were acquired at 300 kV accelerating voltage with 2048 × 2048 slow-scan CCD cameras.

Raman Spectroscopy. Raman spectroscopy was conducted using a NT-MDT NTEGRA Spectra (100x objective) with 532 nm and 633 nm excitation wavelengths at a laser power of 2.38 mW for both wavelengths. Dispersion of G peak (Disp_G) calculations were made from spectra from the same point with the 2 excitation wavelengths. Disp_G is calculated as:

$$\text{Disp}_G = \left| \frac{\text{Pos}(G)_{633 \text{ nm}} - \text{Pos}(G)_{532 \text{ nm}}}{\lambda_{633 \text{ nm}} - \lambda_{532 \text{ nm}}} \right|$$

Where $\text{Pos}(G)$ is the spectral position of the G peak under a given excitation laser and λ is the excitation laser's wavelength. Raman spectra were acquired from 10 randomly distributed points across each NT-3DFG sample with three independently synthesized samples per synthesis condition. Correlation tests were conducted for Disp_G & $I_D I_G^{-1}$ as well as FWHM_G & $I_D I_G^{-1}$ for all synthesis conditions with the equation:⁴⁹

$$r = \frac{\sum(x_i - \bar{x})(y_i - \bar{y})}{\sqrt{\sum(x_i - \bar{x})^2 \sum(y_i - \bar{y})^2}}$$

where r is the coefficient of linear correlation, x is the Disp_G and y is the respective $I_D I_G^{-1}$.

X-ray Photoemission Spectroscopy (XPS). XPS was conducted using an Escalab 250Xi (Thermo Scientific) with Al K α (1486.68 eV) x-ray source at ultra-high vacuum (10^{-9} Torr). Survey spectra were acquired by averaging 5 scans with a 120 eV pass energy, 15 ms acquisition time, and 0.5 eV step size. O1s and C1s spectra were acquired by averaging 10 scans with a 50 eV pass energy, 50 ms acquisition time, and 0.1 eV step size. Compositional and chemical state analyses were completed with Thermo Scientific Avantage software. For the asymmetric shape of the sp^2 peak, a Doniac-Sunjic function was implemented, which is commonly used for spectra of graphite and aromatic molecules.³⁰ XPS analysis was performed for three independently synthesized samples.

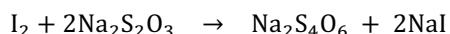
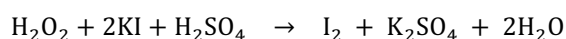
Ultraviolet Photoemission Spectroscopy (UPS). UPS was conducted using an Escalab 250Xi (Thermo Scientific) x with a He I (21.2 eV) source at ultra-high vacuum (10^{-8} Torr.) Valence band spectra were acquired by averaging 10 scans with a 5 eV pass energy, 50 ms acquisition time, and 0.1 eV step size. To measure the secondary electron cut-off energies, valence band spectra were acquired under a 5 V sample bias. The work function was calculated using Thermo Scientific Advantage software. UPS analysis was performed for three independently synthesized samples.

Electrochemical Cell Preparation. Prior to conducting electrochemical testing, contacts composed of 5 nm Cr (99.99%, The R.D. Mathis Co.) followed by 150 nm Au (99.999%, Praxair) were evaporated at the edge of the NT-3DFG samples using a thermal evaporator (Angstrom Thermal Evaporator). Polystyrene wells were then sealed to the NT-3DFG samples using poly dimethyl-siloxane (PDMS) (Sylgard 184 Silicone Elastomer, Dow Corning). Geometric area of NT-3DFG exposed to the electrolyte after adhering the polystyrene well was determined by imaging the sample surfaces at $1\times$ magnification with a stereo microscope (AmScope) and analyzing the images using ImageJ. In order to ensure the interaction of NT-3DFG with the electrolyte, IPA infiltration was conducted, as previously described.¹⁴ 2 mL IPA was introduced into the well, and the sample was placed in a desiccator under vacuum for 5 min. 1.8 mL of IPA was aspirated out and 1.8 mL of DI water was introduced, followed by 5 min in the desiccator under vacuum. This process was repeated four times to exchange IPA with the DI water. A similar procedure was followed to exchange the DI water and 0.1 M KOH (Aqua Solutions, Catalog No. 7220) electrolyte.

Cyclic Voltammetry (CV) testing. CV was performed using a PalmSens3 potentiostat (PalmSens BV) in a three-electrode system with a NT-3DFG sample, Pt wire (CHI115, CH Instruments Inc.), and Ag/AgCl electrode in 3 M KCl (+0.209 V vs. Normal Hydrogen Electrode) (CHI111, CH Instruments Inc.) as the working, counter, and reference electrodes, respectively. Prior to each test, N_2 (99.9999%, Airgas) or O_2 (99.999%, Airgas) was bubbled through the cell for 15 min. CV measurements were recorded with a potential range of 0.2 to -1.2 V versus Ag/AgCl at 50 mV s^{-1} while continuously bubbling N_2 or O_2 through the cell. CV current values for each sample were normalized with respect to the geometric area of each respective sample. The cathodic peak position and current were determined with PStTrace software (PalmSens BV). After the measurements, the sample was washed for 30 min in three DI water baths and

dried overnight in a clean hood. CV testing was conducted for three independently synthesized samples for each NT-3DFG synthesis condition with five scans acquired for every experimental setup.

H₂O₂ Selectivity. The H₂O₂ selectivity of NT-3DFG during oxygen reduction reaction (ORR) was determined by chronoamperometry (CA) and iodometric titration of H₂O₂²⁶ generated in the electrolyte solution. After CV testing, the sample was held at 0.5 V vs. RHE for 1 hour in 0.1 M KOH while bubbling O₂. The current was recorded and integrated to calculate the total number of electrons transferred. After CA, 1.0 ml of the electrolyte, along with 1.0 ml of 2 wt.% potassium iodide (KI) (≥99.0%, Sigma-Aldrich, Catalog No. 221945) solution, 1 ml of 3.5 M sulfuric acid (H₂SO₄) (96%, KMG Electronic Chemical Inc.), and 50 μL of a molybdate catalyst (1 g ammonium molybdate (99.98%, Sigma-Aldrich, Catalog No. 277908) in 10 mL of 6 N ammonium hydroxide (≥99.99%, Sigma-Aldrich, Catalog No. 338818), followed by adding 3 g ammonium nitrate (≥99.5%, Sigma-Aldrich, Catalog No. A7455) and diluting the solution to 50 mL with DI water) were added to a vial. H₂O₂ readily oxidized I⁻ to I₂ under acidic conditions, and the presence of iodine was observed by a characteristic yellow-brown solution color. The solution was then titrated with a 10.000 ± 0.025 mL burette and dropwise additions of a 5 mM sodium thiosulfate (Na₂S₂O₃) (≥ 97.0%, Emplura, Catalog No. 106512) solution. After the solution reaches a straw color, ~5 mg of starch (ACS reagent, Sigma-Aldrich, Catalog No. S9765) is added as an indicator. Titration is complete when the purple color of the starch–iodine complex vanishes to yield a clear solution. The chemical reactions for iodometric titration of H₂O₂ are as follows:



The volume of Na₂S₂O₃ titrated was measured, and the moles of iodine consumed during titration was calculated. One mole of iodine is formed for every mole of H₂O₂ present in the electrolyte solution. The concentration of H₂O₂ in the electrolyte is obtained, and the total amount of H₂O₂ generated is compared to the total charged transferred during CA. H₂O₂ selectivity testing was conducted for three independently synthesized samples.

Rotating disk electrode (RDE) mesh transfer. A NT-3DFG mesh transfer method was developed to transfer NT-3DFG meshes from growth substrates to RDE. Prior to the NT-3DFG synthesis process, a 2 μm-thick SiO₂ layer was deposited on a (100) Si substrate using a Trion Orion PECVD System. NT-3DFG

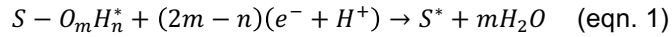
synthesis was performed as stated earlier in the methods section. After synthesis, the sample was placed in a 49% hydrofluoric acid bath for 90 min to etch the SiO₂ layer and lift off the NT-3DFG mesh. The sample was transferred to a DI water bath three times for 10 min each to remove residual HF. Prior to NT-3DFG transfer, the glassy carbon (GC) tip (area: 0.196 cm²) (Pine Research, Catalog No. AFED050P040GC) of a RDE (Pine Research, Catalog No. AFE5TQ050PK) was polished with 0.05 μm alumina slurry (Allied High-Tech Inc., Catalog No. 90-187505) and a microcloth pad (Pine Research, Catalog No. AKPOLISH) until a smooth and reflective surface was achieved. The GC tip was washed three times with DI water then IPA. The NT-3DFG mesh was transferred onto the GC electrode tip and dried for 1 hour in a clean hood. 5 μL of 4:1 volumetric solution of IPA and Nafion (5 wt% Nafion 117, Sigma-Aldrich, Catalog No. 70160) was drop cast onto the surface as a binder, and the electrode was dried for 1 hour in a clean hood.

Rotating disk electrode ORR testing. ORR testing through the RDE setup was conducted using a WaveVortex 10 rotator (Pine Research) and a PalmSens3 potentiostat in a three-electrode setup with NT-3DFG mesh on polished GC tip RDE, graphite electrode (Pine Research, Catalog No. AFCTR3B), and Ag/AgCl electrode in 4 M KCl (+0.199 V vs NHE) (Pine Research, Catalog No. RREF0021) as the working, counter, and reference electrode, respectively. The cell was held in 0.1 M KOH for 1 hour while bubbling N₂ through the electrolyte. CV measurements were recorded with a potential range of 0.2 to -1.2 V versus Ag/AgCl at 50 mV s⁻¹ under N₂ bubbling. O₂ was then bubbled through the cell for 30 min, and CV testing was performed following the same protocol. Then the RDE was slowly ramped up to a rotational speed of 1600 rpm and linear sweep voltammetry (LSV) measurements were made from 0.2 to -1.0 V versus Ag/AgCl at 10 mV s⁻¹. ORR RDE testing was conducted for three NT-3DFG samples independently synthesized at 1100 °C for 120 min. ORR RDE testing was also conducted on the polished GC tip RDE as a control. The mass of NT-3DFG meshes used for ORR RDE testing were calculated through gravimetric analysis with Excellence XS105 Analytical Balance (Mettler Toledo) before and after NT-3DFG synthesis on a substrate of known weight.

Electrochemical stability. The stability of NT-3DFG during ORR was investigated through chronoamperometry. NT-3DFG independently synthesized at 1100 °C for 120 min were held at 0.5 V vs. RHE in 0.1 M KOH while bubbling O₂ through the cell and current was measured as a function of time for 15 hours.

Calculation Details. Density Functional Theory (DFT) calculations were performed using GPAW with the BEEF-vdW exchange-correlation functional using the Atomic Simulation Environment (ASE). Core electrons were described using the Projector Augmented Wave Function (PAW), and k-points were represented using Monkhorst Pack grids. All calculations were done with a grid spacing of 0.18 Å and converged with a force criterion of $< 0.05 \text{ eV } \text{Å}^{-1}$. A $6 \times 6 \times 1$ k-point grid was used for a unit cell having 6 atoms each in the x and y directions. The free energies of oxygen intermediates were calculated using DFT, at standard conditions, and at a potential of 0 V versus the RHE by incorporating entropy contributions and zero-point energy. The effect of potential U is included by shifting the free energy of an electron by $-eU$. For every DFT calculation, we additionally leverage built-in error estimation capabilities within the BEEF-vdW XC-functional which creates an ensemble of energies, from which the predictive confidence of the calculation may be inferred. This error estimation capability has been previously used to describe the uncertainty in predicting magnetic ground states, reaction mechanism pathways, heterogeneous catalytic activity, and solid state properties.

Catalyst Active Site Characterization through Pourbaix Diagrams. The surface Pourbaix diagram represents the stable state of the catalyst surface in electrochemical systems as a function of pH and electrode potential U . Consider an edge site S with adsorption site $*$ in its pristine state. A generalized representation of the adsorption of oxygenated intermediates, denoted as $O_mH_n^*$, can be written as



where m and n are the number of oxygen and hydrogen atoms in the adsorbate respectively. Note that this representation corresponds to a concerted proton-coupled electron transfer (PCET) reaction. The associated free energy change can be computed as:

$$\Delta G(U, pH) = G_{S^*} + mG_{H_2O} - G_{S-O_mH_n^*} - (2m - n)(G_{e^-} + G_{H^+}) \quad (\text{eqn. 2})$$

Rewriting Eqn. 2, the free energy of electrons G_{e^-} is defined as $-eU$ where e is the electron charge. The free energy of protons G_{H^+} is determined from the computational hydrogen electrode using the equilibrium relation $H^+ + e^- \rightarrow H_2$. This gives at non-standard conditions $G_{H^+} + G_{e^-} = \frac{1}{2}G_{H_2} - eU_{SHE} + k_B T (\ln[a_{H^+}])$, where U_{SHE} is the potential relative to the standard hydrogen electrode (SHE). We then write the free energy change for adsorption of $O_mH_n^*$ intermediates as

$$\Delta G(U, pH) = G_{S^*} + mG_{H_2O} - G_{S-O_{mH_n^*}} - (2m - n)\left(\frac{1}{2}G_{H_2} - eU_{SHE} - 2.303 k_B T pH\right) \text{ (eqn. 3)}$$

Therefore, we can derive a relation between potential and pH for a wide variety of adsorbates on a surface S in reference to standard conditions when $\Delta G(U, pH) = 0$.

Since the most stable state at a given condition is that which minimizes free energy, we determine the surface Pourbaix diagram by choosing the appropriate state at each set of conditions of U and pH . The phase transitions between adsorbates appear as lines with a slope of -59 mV/pH at standard conditions. Free energies are determined from calculated energies of adsorption E_{S^*} corrected for entropy, S , and zero-point energies, ZPE , which we assume do not change significantly with temperature, by $\Delta G = \Delta E_{ref, H_2O} - T\Delta S + \Delta ZPE$. Values for entropy and zero-point energy correction are given in the Supporting Information. In this work, we assume constant zero-point energies across the ensemble of functionals for simplicity, since it is expected to have negligible variation (of order $k_B T$, where k_B is the Boltzmann constant) relative to the order of magnitude ($10\text{-}20 k_B T$) of the surface energetics.

Bayesian Error Estimation Framework. With the recent development of the Bayesian Ensemble Error Functional with van der Waals correlations (BEEF-vdW), there exists a systematic approach to estimate the uncertainty in energetics of a DFT calculation. BEEF-vdW is a semi-empirical exchange correlation (XC) functional including non-local contributions, developed by using training data sets for molecular formation energies, molecular reaction energies, molecular reaction barriers, non-covalent interactions, solid state properties, and chemisorption on solid surfaces.

The exchange correlation energy in BEEF-vdW is expressed as a sum of the GGA exchange energy expanded using Legendre polynomials, the LDA and PBE correlation energies and the non-local correlation energy from vdW-DF2.^{50, 51} The error estimation functionality is enabled by deriving an ensemble of energies from an ensemble of exchange correlation functionals non-self-consistently following a self-consistent DFT calculation. The ensemble of exchange correlation functionals is generated using a probability distribution function for the parameters a_m and α_c such that the standard deviation of the ensemble of energies reproduces the standard deviation for the training properties calculated using BEEF-vdW self-consistently.

Prediction Confidence of Surface Pourbaix Diagrams. Pourbaix diagrams typically depict only the most stable state of the surface (minimum Gibbs free energy) over a range of operating potentials (U) and

pH values with sharp phase boundaries. We utilize error estimation capabilities within the BEEF-vdW exchange correlation functional to create an ensemble of Pourbaix diagrams, allowing us to apply statistical tools to obtain a measure of the confidence in a predicted surface state by quantifying the agreement between functionals. We are interested in determining the level of agreement between functionals at the GGA-level as to the most energetically favorable surface state as a function of potential and *pH*. We use the confidence-value (c-value),³⁹ which in this context is defined as the fraction of the ensemble that is in agreement with the hypothesis of the optimal BEEF-vdW (best-fit) functional.

References

1. Campos-Martin, J. M., Blanco-Brieva, G., Fierro, J. L. G. Hydrogen peroxide synthesis: An outlook beyond the anthraquinone process. *Angew. Chem. Int. Ed.* **45**, 6962-6984 (2006).
2. Chen, Z., Chen, S., Siahrostami, S., Chakthranont, P., Hahn, C., Nordlund, D., Dimosthenis, S., Nørskov, J. K., Bao, Z., Jaramillo, T. F. Development of a reactor with carbon catalysts for modular-scale, low-cost electrochemical generation of H₂O₂. *React. Chem. Eng.* **2**, 239-245 (2017).
3. Seh, Z. W., Kibsgaard, J., Dickens, C. F., Chorkendorff, I., Nørskov, J. K., Jaramillo, T. F. Combining theory and experiment in electrocatalysis: Insights into materials design. *Science* **355**, eaad4998 (2017).
4. Siahrostami, S., Verdaguer-Casadevall, A., Karamad, M., Deiana, D., Malacrida, P., Wickman, B., Escudero-Escribano, M., Paoli, E. A., Frydendal, R., Hansen, T. W., Chorkendorff, I., Stephens, I. E. L., Rossmeisl, J. Enabling direct H₂O₂ production through rational electrocatalyst design. *Nat. Mater.* **12**, 1137 (2013).
5. Verdaguer-Casadevall, A., Deiana, D., Karamad, M., Siahrostami, S., Malacrida, P., Hansen, T. W., Rossmeisl, J., Chorkendorff, I., Stephens, I. E. L. Trends in the electrochemical synthesis of H₂O₂: Enhancing activity and selectivity by electrocatalytic site engineering. *Nano Lett.* **14**, 1603-1608 (2014).
6. Lu, Z., Chen, G., Siahrostami, S., Chen, Z., Liu, K., Xie, J., Liao, L., Wu, T., Lin, D., Liu, Y., Jaramillo, T. F., Nørskov, J. K., Cui, Y. High-efficiency oxygen reduction to hydrogen peroxide catalysed by oxidized carbon materials. *Nat. Catal.* **1**, 156-162 (2018).
7. Chen, S., Chen, Z., Siahrostami, S., Kim, T. R., Nordlund, D., Sokaras, D., Nowak, S., To, J. W. F., Higgins, D., Sinclair, R., Nørskov, J. K., Jaramillo, T. F., Bao, Z. Defective carbon-based materials for the electrochemical synthesis of hydrogen peroxide. *ACS Sustain. Chem. Eng.* **6**, 311-317 (2018).
8. Won Kim, H., Ross, M., Kornienko, N., Zhang, L., Guo, J., Yang, P., McCloskey, B. Efficient hydrogen peroxide generation using reduced graphene oxide-based oxygen reduction electrocatalysts. *Nat. Catal.* **1**, 282-290 (2018).
9. Hansen, H. A., Rossmeisl, J., Nørskov, J. K. Surface pourbaix diagrams and oxygen reduction activity of Pt, Ag and Ni (111) surfaces studied by DFT. *PCCP* **10**, 3722-3730 (2008).
10. Krishnamurthy, D., Sumaria, V., Viswanathan, V. Maximal predictability approach for identifying the right descriptors for electrocatalytic reactions. *J. Phys. Chem. Lett.* **9**, 588-595 (2018).
11. Kang, Y., Yang, P., Markovic, N. M., Stamenkovic, V. R. Shaping electrocatalysis through tailored nanomaterials. *Nano Today* **11**, 587-600 (2016).
12. Montoya, J. H., Seitz, L. C., Chakthranont, P., Vojvodic, A., Jaramillo, T. F., Nørskov, J. K. Materials for solar fuels and chemicals. *Nat. Mater.* **16**, 70 (2016).
13. Bockris, J. O. M., Khan, S. U. *Surface electrochemistry: A molecular level approach*. (Springer Science & Business Media, 2013).
14. Garg, R., Rastogi, S. K., Lamparski, M., de la Barrera, S., Pace, G. T., Nuhfer, N. T., Hunt, B. M., Meunier, V., Cohen-Karni, T. Nanowire-mesh templated growth of out-of-plane three-dimensional fuzzy graphene. *ACS Nano* **11**, 6301-6311 (2017).
15. Bo, Z., Yang, Y., Chen, J., Yu, K., Yan, J., Cen, K. Plasma-enhanced chemical vapor deposition synthesis of vertically oriented graphene nanosheets. *Nanoscale* **5**, 5180-5204 (2013).
16. Ghosh, S., Polaki, S. R., Kumar, N., Amirthapandian, S., Kamruddin, M., Ostrikov, K. K. Process-specific mechanisms of vertically oriented graphene growth in plasmas. *Beilstein J. Nanotechnol.* **8**, 1658-1670 (2017).
17. Döbbelin, M., Ciesielski, A., Haar, S., Osella, S., Bruna, M., Minoia, A., Grisanti, L., Mosciatti, T., Richard, F., Prasetyanto, E. A. Light-enhanced liquid-phase exfoliation and current photoswitching in graphene-azobenzene composites. *Nat. Commun.* **7**, 11090 (2016).
18. Ferrari, A. C., Robertson, J. Resonant raman spectroscopy of disordered, amorphous, and diamondlike carbon. *Phys. Rev. B* **64**, 075414 (2001).
19. Torrisi, F., Hasan, T., Wu, W., Sun, Z., Lombardo, A., Kulmala, T. S., Hsieh, G.-W., Jung, S., Bonaccorso, F., Paul, P. J., Chu, D., Ferrari, A. C. Inkjet-printed graphene electronics. *ACS Nano* **6**, 2992-3006 (2012).
20. Ferrari, A. C., Basko, D. M. Raman spectroscopy as a versatile tool for studying the properties of graphene. *Nat. Nanotechnol.* **8**, 235 (2013).

21. Cançado, L. G., Jorio, A., Ferreira, E. H. M., Stavale, F., Achete, C. A., Capaz, R. B., Moutinho, M. V. O., Lombardo, A., Kulmala, T. S., Ferrari, A. C. Quantifying defects in graphene via raman spectroscopy at different excitation energies. *Nano Lett.* **11**, 3190-3196 (2011).
22. Casiraghi, C., Hartschuh, A., Qian, H., Piscanec, S., Georgi, C., Fasoli, A., Novoselov, K. S., Basko, D. M., Ferrari, A. C. Raman spectroscopy of graphene edges. *Nano Lett.* **9**, 1433-1441 (2009).
23. Dimovski, S., Nikitin, A., Ye, H., Gogotsi, Y. Synthesis of graphite by chlorination of iron carbide at moderate temperatures. *J. Mater. Chem.* **14**, 238-243 (2004).
24. Meyer, J. C., Geim, A. K., Katsnelson, M. I., Novoselov, K. S., Booth, T. J., Roth, S. The structure of suspended graphene sheets. *Nature* **446**, 60 (2007).
25. Gong, K., Du, F., Xia, Z., Durstock, M., Dai, L. Nitrogen-doped carbon nanotube arrays with high electrocatalytic activity for oxygen reduction. *Science* **323**, 760-764 (2009).
26. McCloskey, B. D., Valery, A., Luntz, A. C., Gowda, S. R., Wallraff, G. M., Garcia, J. M., Mori, T., Krupp, L. E. Combining accurate O₂ and Li₂O₂ assays to separate discharge and charge stability limitations in nonaqueous Li-O₂ batteries. *J. Phys. Chem. Lett.* **4**, 2989-2993 (2013).
27. Luo, Z., Lim, S., Tian, Z., Shang, J., Lai, L., MacDonald, B., Fu, C., Shen, Z., Yu, T., Lin, J. Pyridinic N doped graphene: Synthesis, electronic structure, and electrocatalytic property. *J. Mater. Chem.* **21**, 8038-8044 (2011).
28. Heimann, P., Neddermeyer, H., Roloff, H. Ultraviolet photoemission for intrinsic surface states of the noble metals. *J. Phys. C: Solid State Phys.* **10**, L17 (1977).
29. Yu, Y.-J., Zhao, Y., Ryu, S., Brus, L. E., Kim, K. S., Kim, P. Tuning the graphene work function by electric field effect. *Nano Lett.* **9**, 3430-3434 (2009).
30. Díaz, J., Paolicelli, G., Ferrer, S., Comin, F. Separation of the sp³ and sp² components in the C1s photoemission spectra of amorphous carbon films. *Phys. Rev. B* **54**, 8064-8069 (1996).
31. Yang, D., Velamakanni, A., Bozoklu, G., Park, S., Stoller, M., Piner, R. D., Stankovich, S., Jung, I., Field, D. A., Ventrice, C. A., Ruoff, R. S. Chemical analysis of graphene oxide films after heat and chemical treatments by x-ray photoelectron and micro-raman spectroscopy. *Carbon* **47**, 145-152 (2009).
32. Pourbaix, M., Van Muylder, J., De Zoubov, N. Electrochemical properties of the platinum metals. *Platinum Met. Rev.* **3**, 47-53 (1959).
33. Hansen, H. A., Man, I. C., Studt, F., Abild-Pedersen, F., Bligaard, T., Rossmeisl, J. Electrochemical chlorine evolution at rutile oxide (110) surfaces. *PCCP* **12**, 283-290 (2010).
34. Exner, K. S., Anton, J., Jacob, T., Over, H. Chlorine evolution reaction on RuO₂ (110): Ab initio atomistic thermodynamics study-pourbaix diagrams. *Electrochim. Acta* **120**, 460-466 (2014).
35. Exner, K. S. Constrained ab initio thermodynamics: Transferring the concept of surface pourbaix diagrams in electrocatalysis to electrode materials in lithium-ion batteries. *ChemElectroChem* **4**, 3231-3237 (2017).
36. Exner, K. S. A short perspective of modeling electrode materials in lithium-ion batteries by the ab initio atomistic thermodynamics approach. *J. Solid State Electrochem.* **22**, 3111-3117 (2018).
37. Christensen, R., Hummelshøj, J. S., Hansen, H. A., Vegge, T. Reducing systematic errors in oxide species with density functional theory calculations. *J. Phys. Chem. C* **119**, 17596-17601 (2015).
38. Christensen, R., Hansen, H. A., Dickens, C. F., Nørskov, J. K., Vegge, T. Functional independent scaling relation for ORR/OER catalysts. *J. Phys. Chem. C* **120**, 24910-24916 (2016).
39. Krishnamurthy, D., Sumaria, V., Viswanathan, V. Quantifying robustness of DFT predicted pathways and activity determining elementary steps for electrochemical reactions. *J. Phys. Chem.* **150**, 041717 (2019).
40. Koper, M. T. Thermodynamic theory of multi-electron transfer reactions: Implications for electrocatalysis. *J. Electroanal. Chem.* **660**, 254-260 (2011).
41. Calle-Vallejo, F., Koper, M. T. First-principles computational electrochemistry: Achievements and challenges. *Electrochim. Acta* **84**, 3-11 (2012).
42. Viswanathan, V., Hansen, H. A., Rossmeisl, J., Nørskov, J. K. Unifying the 2e⁻ and 4e⁻ reduction of oxygen on metal surfaces. *J. Phys. Chem. Lett.* **3**, 2948-2951 (2012).
43. Hansen, H. A., Viswanathan, V., Nørskov, J. K. Unifying kinetic and thermodynamic analysis of 2 e⁻ and 4 e⁻ reduction of oxygen on metal surfaces. *J. Phys. Chem. C* **118**, 6706-6718 (2014).
44. Son, Y.-W., Cohen, M. L., Louie, S. G. Half-metallic graphene nanoribbons. *Nature* **444**, 347 (2006).
45. Okada, S. Energetics of nanoscale graphene ribbons: Edge geometries and electronic structures. *Phys. Rev. B* **77**, 041408 (2008).

46. Cohen-Karni, T., Timko, B. P., Weiss, L. E., Lieber, C. M. Flexible electrical recording from cells using nanowire transistor arrays. *Proc. Natl. Acad. Sci. U.S.A.* **106**, 7309-7313 (2009).
47. Arrhenius, S. Über die dissociationswärme und den einfluss der temperatur auf den dissociationsgrad der elektrolyte. *Z. Phys. Chem.* **4**, 96-116 (1889).
48. Canny, J. A computational approach to edge detection. *IEEE Trans. Pattern Anal. Mach. Intell.* **8**, 679-698 (1986).
49. Taylor, J. *Introduction to error analysis, the study of uncertainties in physical measurements*, 2nd edn. (University Science Books: Mill Valley, CA, 1997).
50. Perdew, J. P., Burke, K., Ernzerhof, M. Generalized gradient approximation made simple. *Phys. Rev. Lett.* **77**, 3865 (1996).
51. Lee, K., Murray, É. D., Kong, L., Lundqvist, B. I., Langreth, D. C. Higher-accuracy van der waals density functional. *Phys. Rev. B* **82**, 081101 (2010).

Supporting Information for

Engineering Three-Dimensional (3D) Out-of-Plane Graphene Edge Sites for Highly-Selective Two-Electron Oxygen Reduction Electrocatalysis

San Roman, D.,^{1^} Krishnamurthy, D.,^{2^} Garg, R.,¹ Nuhfer, N.,¹ Viswanathan, V.,^{2*} Cohen-Karni, T.^{1,3,*}

¹ Department of Material Science and Engineering, Carnegie Mellon University, Pittsburgh, Pennsylvania, 15213, USA.

² Department of Mechanical Engineering, Carnegie Mellon University, Pittsburgh, Pennsylvania, 15213, USA.

³ Department of Biomedical Engineering, Carnegie Mellon University, Pittsburgh, Pennsylvania, 15213, USA.

[^] Equal Contribution

^{*} Corresponding author

Table of Contents

Figure S1	NT-3DFG growth kinetics
Figure S2	Effects of NT-3DFG synthesis time
Figure S3	Raman analysis of edge and bulk defects
Figure S4	Tunable morphology of NT-3DFG edges
Figure S5	Analysis of ORR CV response of NT-3DFG
Figure S6	Electrons transferred during ORR
Figure S7	Morphology of NT-3DFG before & after ORR
Figure S8	Raman spectroscopy of NT-3DFG after ORR
Figure S9	Valence states and work function measurement of NT-3DFG
Figure S10	Edge Detection for NT-3DFG
Figure S11	Determining the state of the surface of AC edge sites
Figure S12	Determining the state of the surface of ZZ edge sites
Figure S13	Confidence values associated with predictions of the surface state of AC edge sites
Figure S14	Confidence values associated with predictions of the surface state of ZZ edge sites
Figure S15	Theoretical activity volcano for 2-electron ORR at graphene edge sites
Figure S16	Distributions of coefficients in the structure-property relationship
Table S1	Data summary for NT-3DFG Raman analysis
Table S2-6	Data summary for NT-3DFG dual-laser Raman analysis
Table S7	Data summary for H ₂ O ₂ selectivity of NT-3DFG
Table S8	Data summary for NT-3DFG Raman analysis after ORR
Table S9	Data summary for XPS analysis of NT-3DFG before & after ORR.
Table S10	Data summary for C1s & O1s chemical states of NT-3DFG after ORR
Table S11	Data summary for explored ZZ & AC active sites with local coordination environment

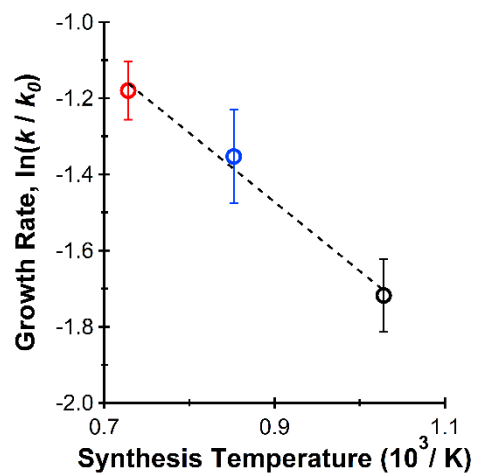


Figure S1. NT-3DFG growth kinetics. Arrhenius plot for NT-3DFG growth at 700, 900, and 1100 °C (black, blue, and red, respectively.)

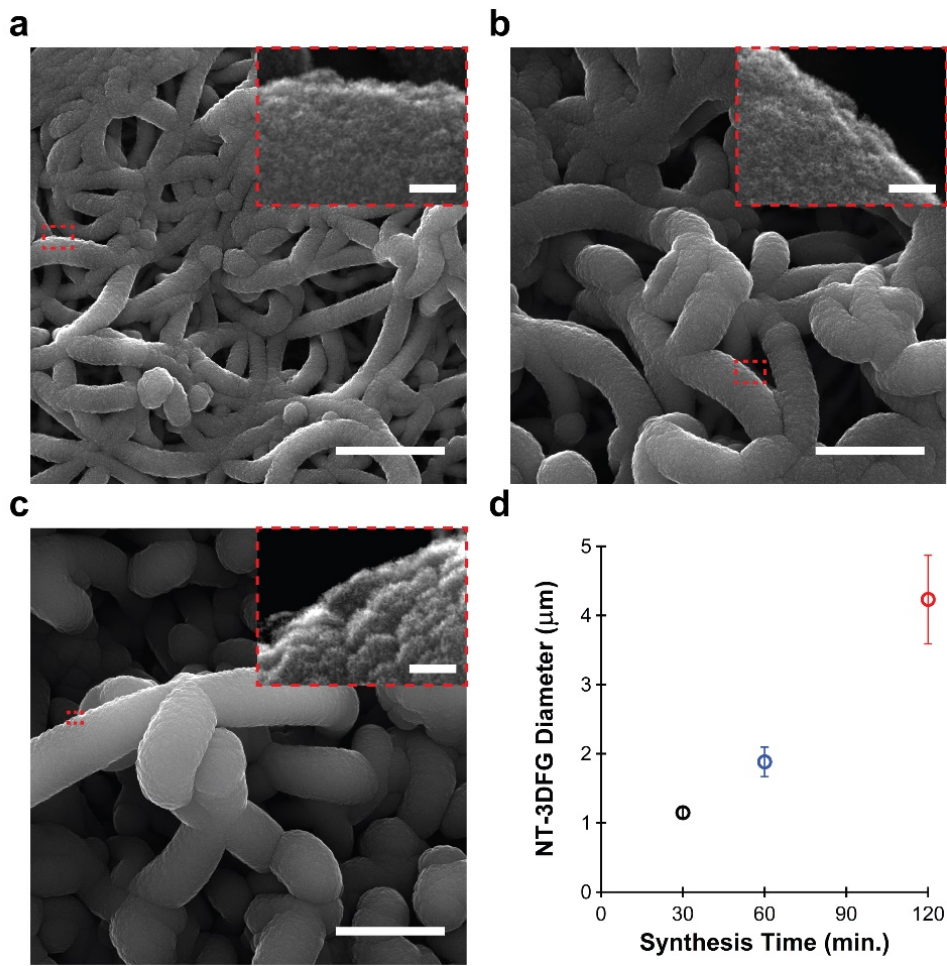


Figure S2. Effects of NT-3DFG synthesis time. (a-c) SEM images of NT-3DFG synthesized for 30, 60, 120 minutes at 1100 °C, respectively. Scale bars: 5, 5, and 10 μm, respectively. Insets represented by red dashed boxes show out-of-plane graphene on SiNW. Inset scale bars: 300 nm. (d) NT-3DFG diameter as a function of synthesis time at 1100 °C. Results are presented as mean ± standard deviation.

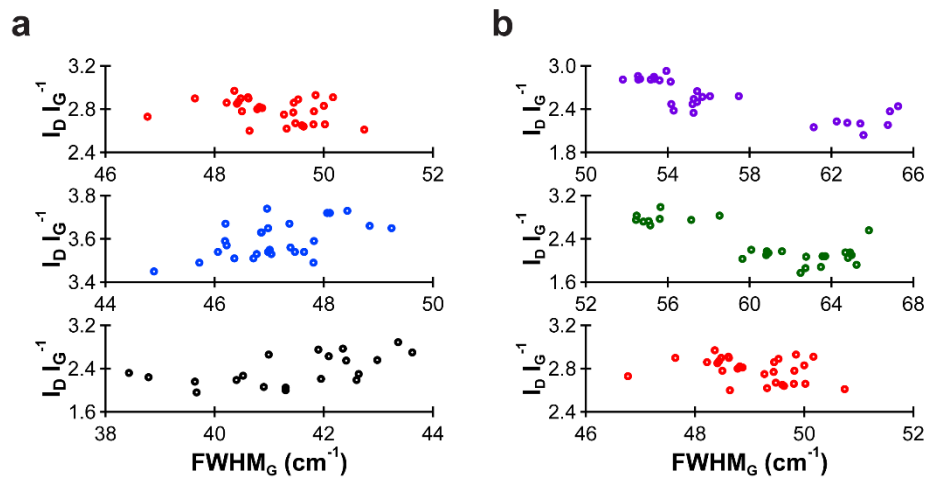
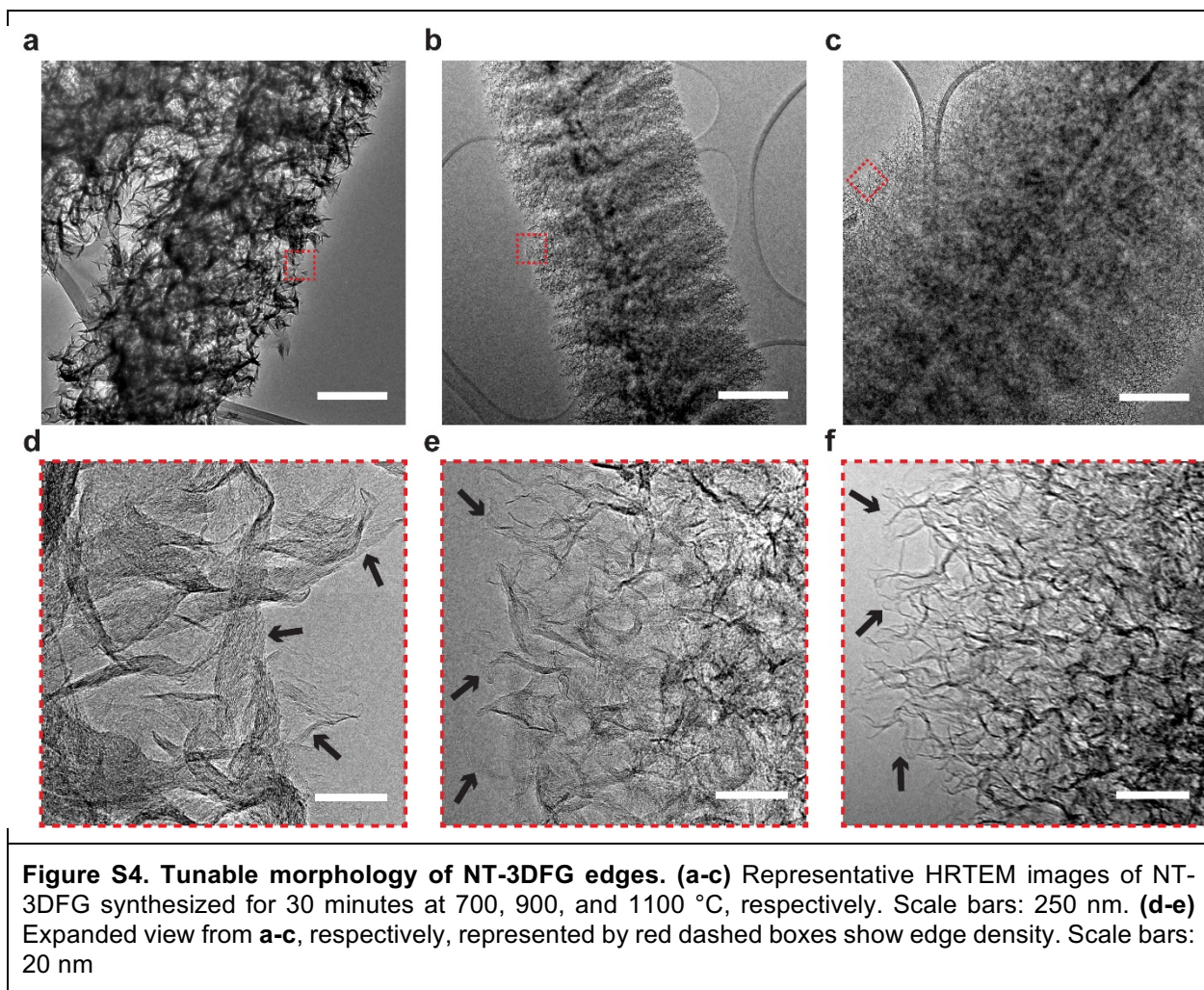


Figure S3. Raman analysis of edge and bulk defects. $I_D I_G^{-1}$ as a function of $FWHM_G$ for NT-3DFG synthesized at (a) 700 (**black**), 900 (**blue**), and 1100 °C (**red**) for 30 min; and (b) 1100 °C for 30 (**red**), 60 (**green**), and 120 min (**purple**).



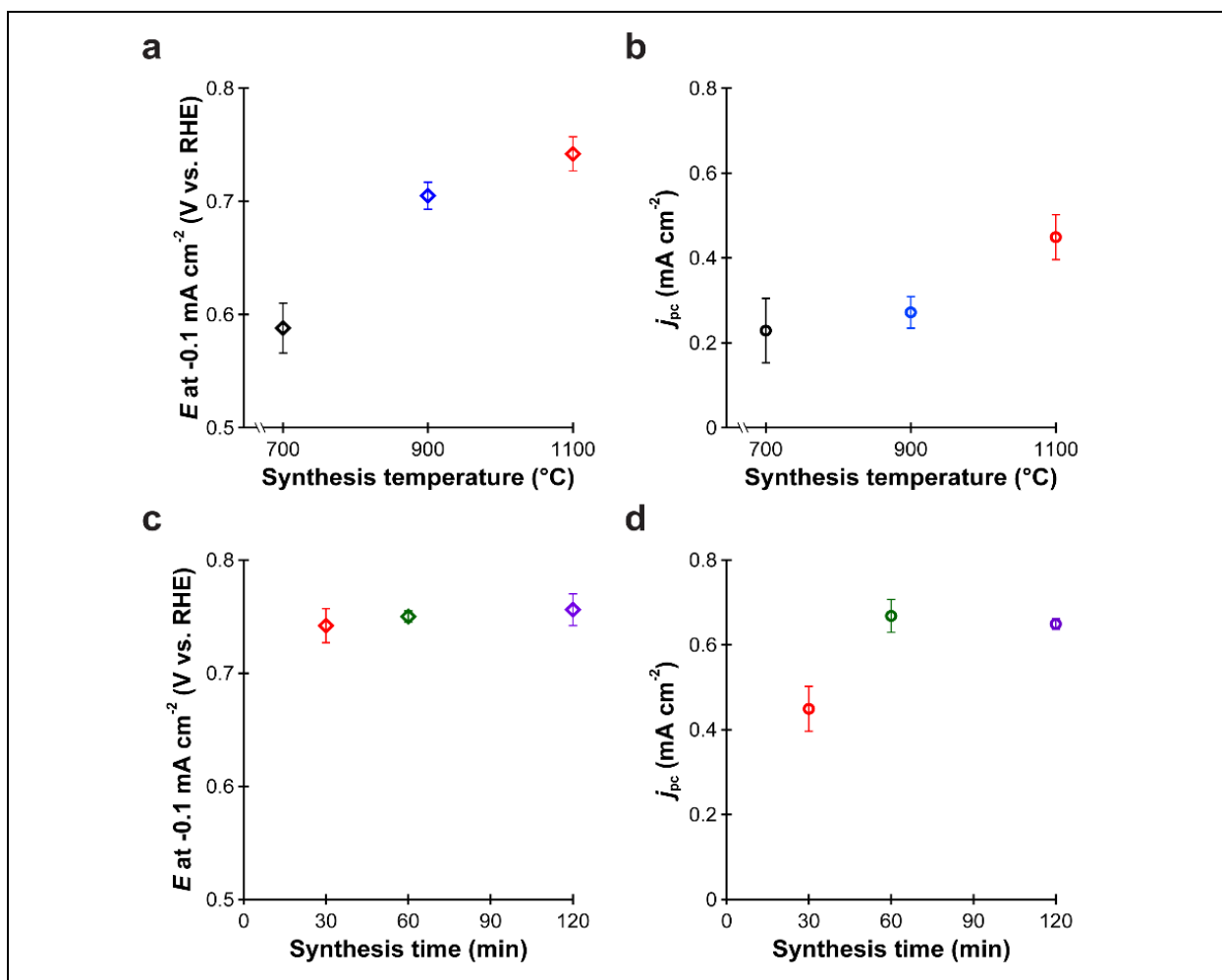


Figure S5. Analysis of ORR CV response of NT-3DFG. (a) Potential at -0.1 mA/cm^2 and (b) baseline-subtracted peak cathodic current density (j_{pc}) for NT-3DFG synthesized for 30 min. as a function of synthesis temperature: 700 (black), 900 (blue), and 1100 $^{\circ}\text{C}$ (red). (c) Potential at -0.1 mA/cm^2 and (d) j_{pc} for NT-3DFG synthesized at 1100 $^{\circ}\text{C}$ as a function of synthesis time: 30 (red), 60 (green), and 120 (purple) minutes. CV was conducted in 0.1 M KOH while bubbling O_2 at a scan rate of 50 mV/s.

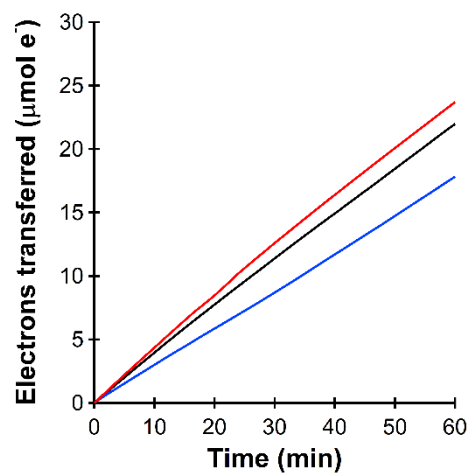


Figure S6. Electrons transferred during ORR. Total electrons transferred ($\mu\text{mol e}^-$) for three independent electrodes (**red, black, & blue.**) as a function of process time. Testing was conducted for 1 hour at 0.5 V vs. RHE in 0.1 M KOH while bubbling O_2 .

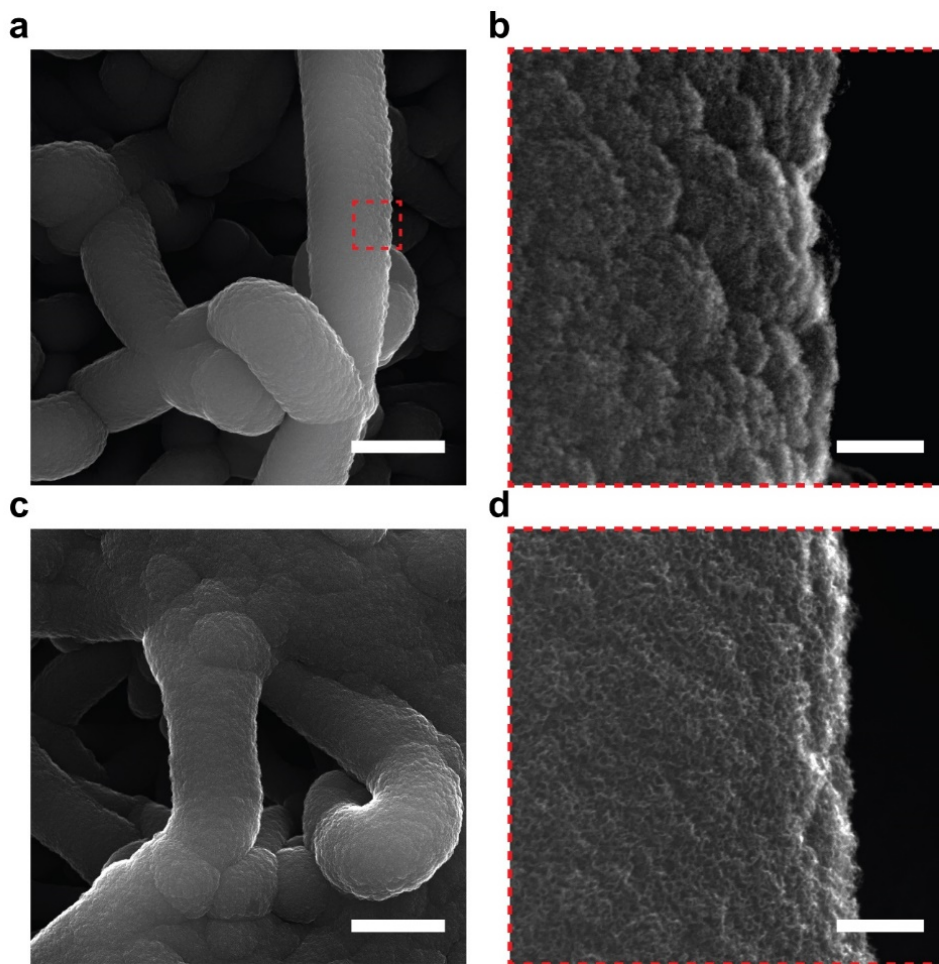


Figure S7. Morphology of NT-3DFG before & after ORR. (a) NT-3DFG before ORR testing. (b) Expanded view from (a) represented by red dashed boxes show edges of 3DFG. (c) NT-3DFG after ORR CV and H₂O₂ selectivity testing. (d) Expanded view from (c) represented by red dashed boxes show edges of 3DFG. Scale bars: 3 μm (a,c) and 300 nm (b,d). NT-3DFG was synthesized at 1100 $^{\circ}\text{C}$ for 120 minutes.

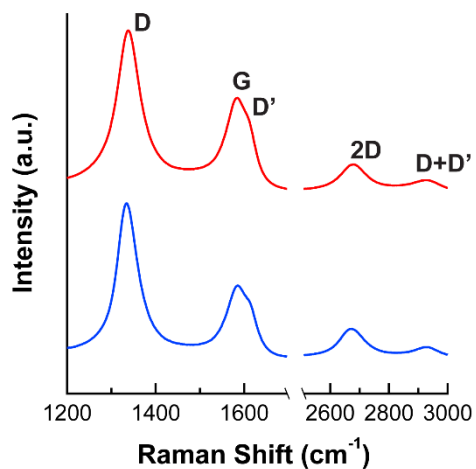


Figure S8. Raman spectroscopy of NT-3DFG before & after ORR. (a) Raman spectra of NT-3DFG before ORR testing (**blue**) and NT-3DFG after ORR CV and H₂O₂ selectivity testing (**red**.) NT-3DFG was synthesized at 1100 °C for 120 minutes.

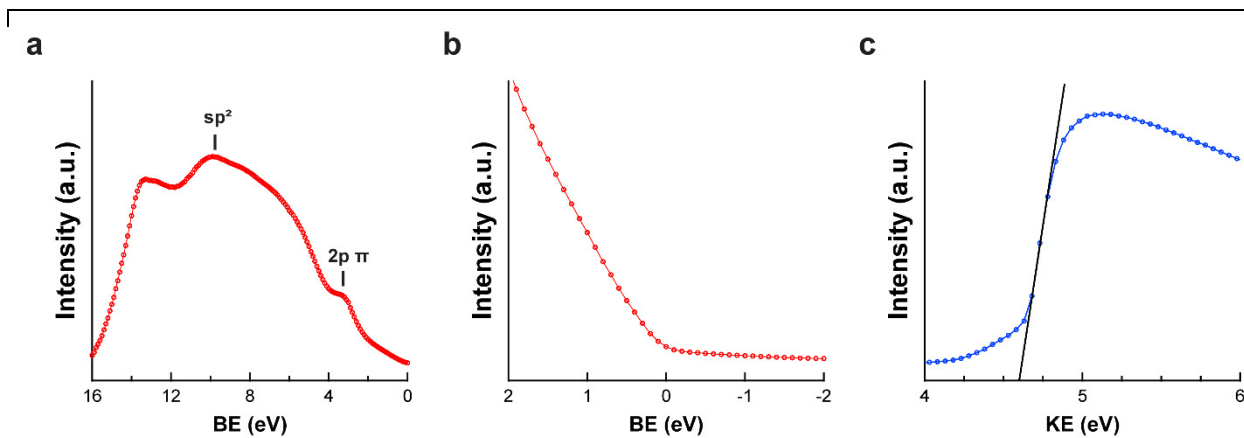


Figure S9. Valence states and work function of NT-3DFG. (a) Representative ultraviolet photoemission (UPS) for NT-3DFG. (b) Photoemission from states near the Fermi energy (c) Secondary cutoff edge for NT-3DFG under a 5 V sample bias. NT-3DFG was synthesized at 1100 °C for 120 minutes.

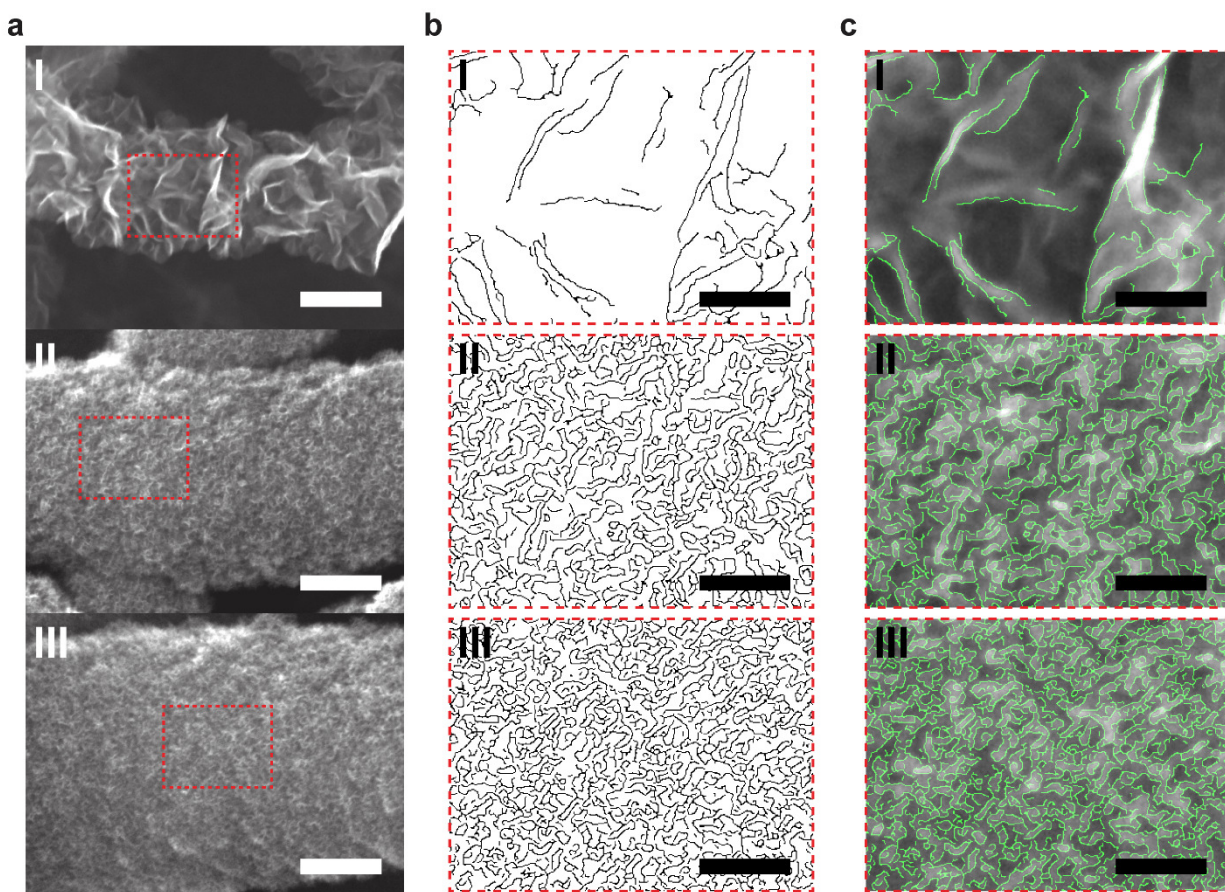


Figure S10. Edge Detection of NT-3DFG. (a) Representative SEM images of NT-3DFG synthesized for 30 minutes at 700, 900, and 1100 °C, (a.I-III, respectively.) Scale bars: 300 nm. (b) Expanded views of images (a.I-III) denoted by dashed red lines showing respective edge maps (b.I-III) of NT-3DFG. Scale bars: 100 nm. (c) Superimposed edge maps (b.I-III, green) on corresponding SEM images (a.I-III, greyscale). Scale bars: 100 nm.

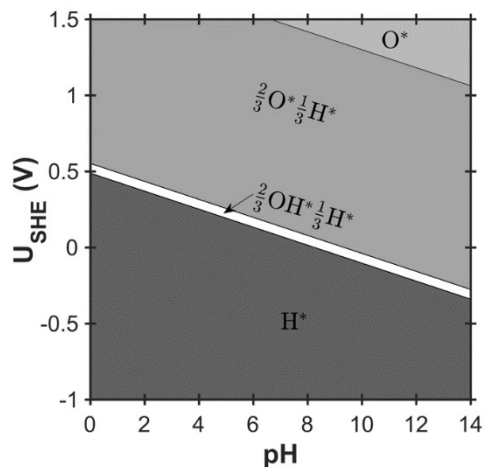


Figure S11. Determining the state of the surface of AC edge sites. Pourbaix diagram showing the most energetically favorable surface species configuration of AC edge sites, as a function of reaction conditions of electrode potential and pH, predicted from the optimal BEEF-vdW exchange correlation functional. Our analysis suggests that for sites that exhibit activity below ≈ 0.5 V, the surface is hydrogen saturated.

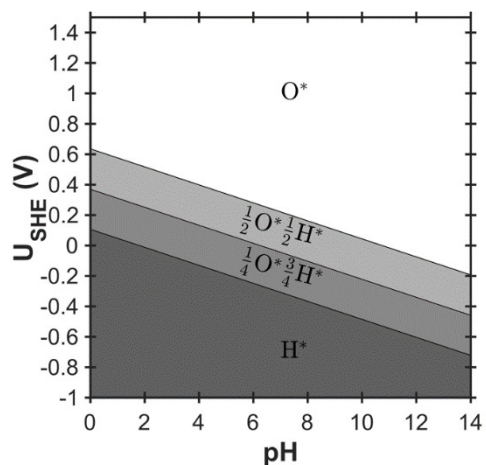


Figure S12. Determining the state of the surface of ZZ edge sites. Pourbaix diagram showing the most energetically favorable surface species configuration of ZZ edge sites, as a function of reaction conditions of electrode potential and pH, predicted from the optimal BEEF-vdW exchange correlation functional. Our analysis suggests that all active sites of interest under operating conditions are oxygen saturated.

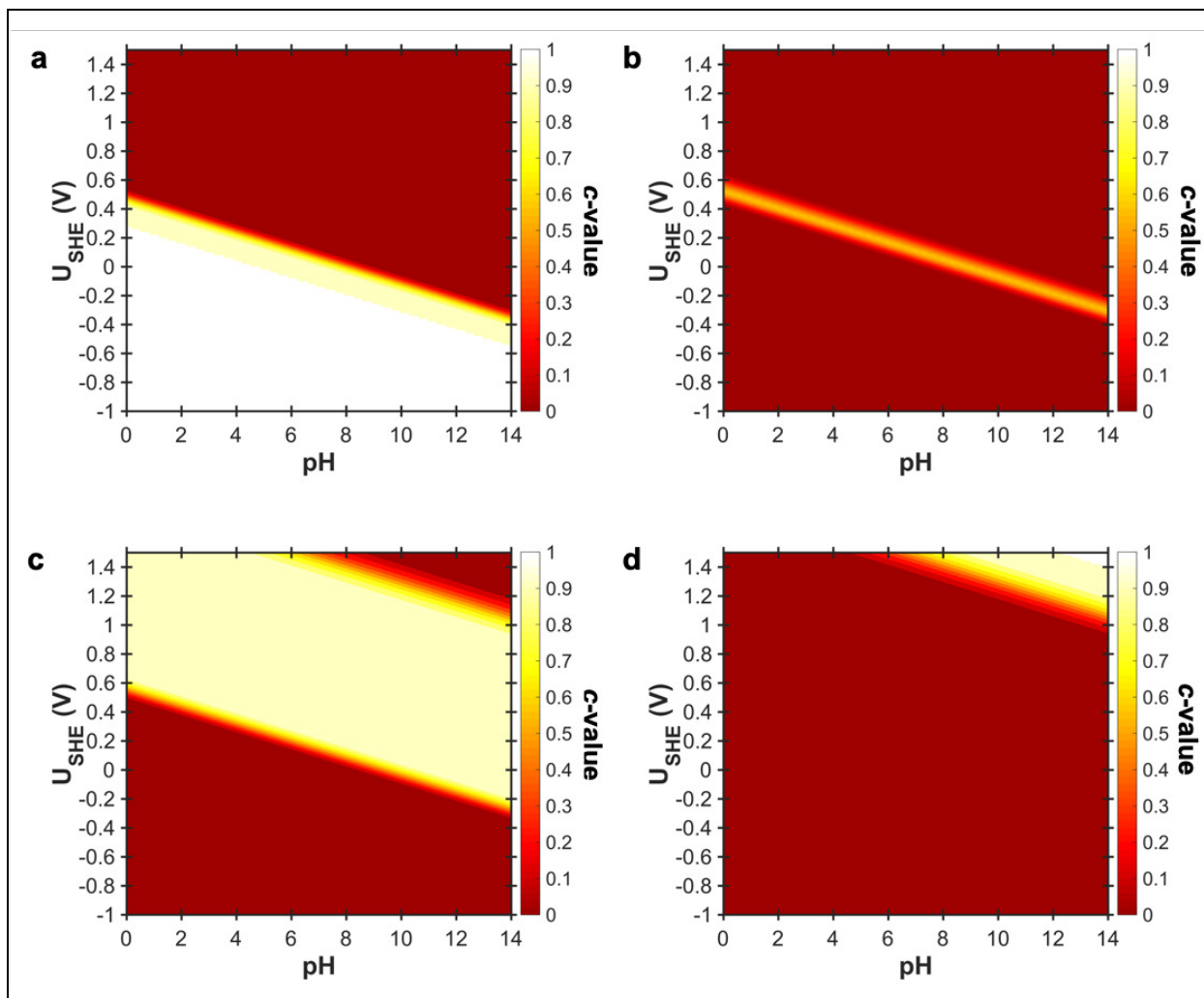


Figure S13. Confidence values associated with predictions of the surface state of AC edge sites through a Pourbaix diagram. Confidence values shown correspond to the surface states corresponding to (a) H^* , (b) $\frac{2}{3}OH^* - \frac{1}{3}H^*$, (c) $\frac{2}{3}O^* - \frac{1}{3}H^*$, and (d) O^* , which appear in the Pourbaix diagram as predicted using the optimal BEEF-vdW exchange correlation functional. The color bar indicates the associated confidence value (c-value) with the predicted surface state, which quantifies the degree of agreement between exchange correlation functionals at the chosen level of DFT complexity.

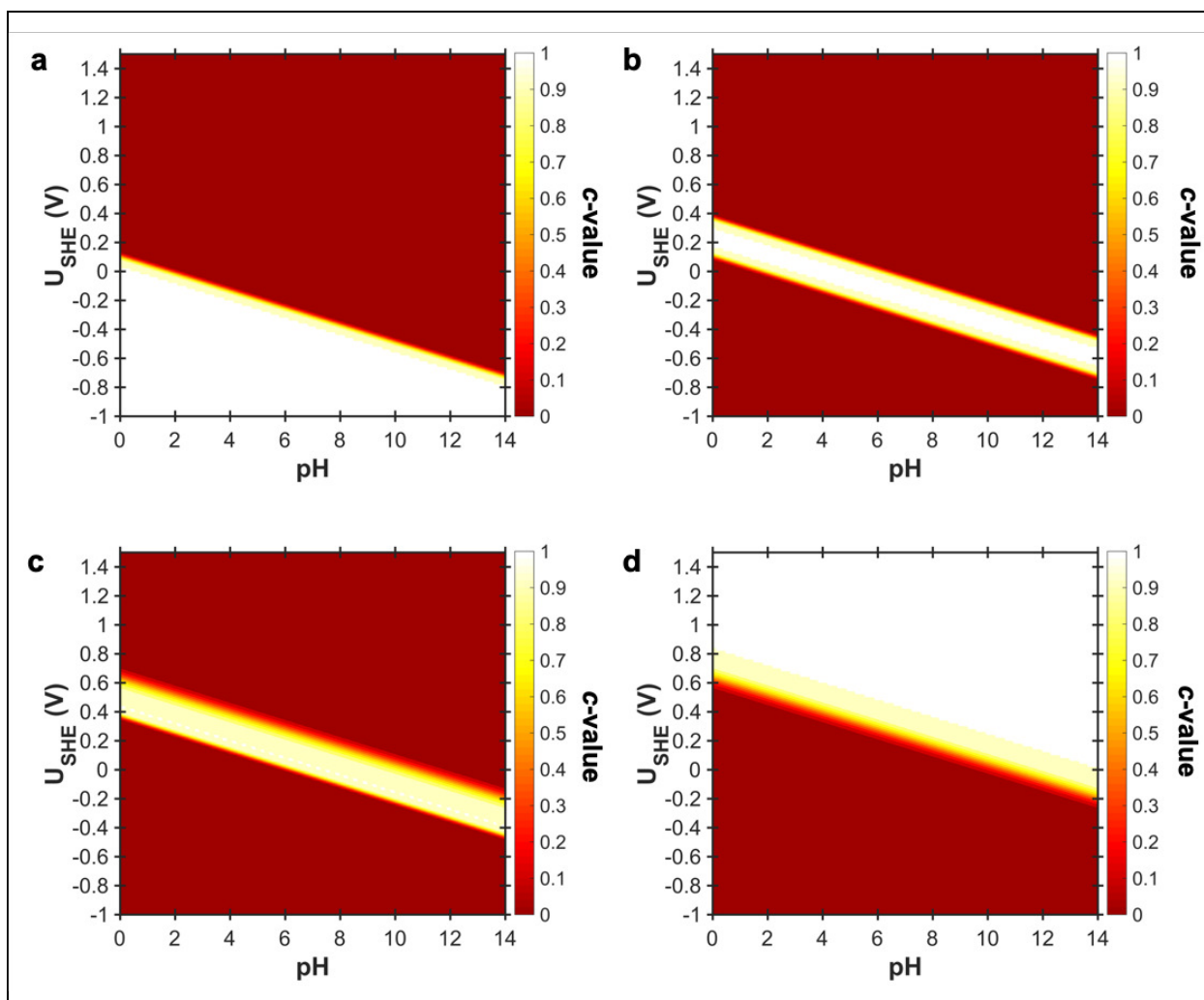


Figure S14. Confidence values associated with predictions of the surface state of ZZ edge sites through a Pourbaix diagram. Confidence values shown correspond to the surface states corresponding to (a) H^* , (b) $\frac{1}{4}\text{O}^{*3/4}\text{H}^*$, (c) $\frac{1}{2}\text{O}^{*1/2}\text{H}^*$, and (d) O^* , which appear in the Pourbaix diagram as predicted using the optimal BEEF-vdW exchange correlation functional. The color bar indicates the associated confidence value (c-value) with the predicted surface state, which quantifies the degree of agreement between exchange correlation functionals at the chosen level of DFT complexity.

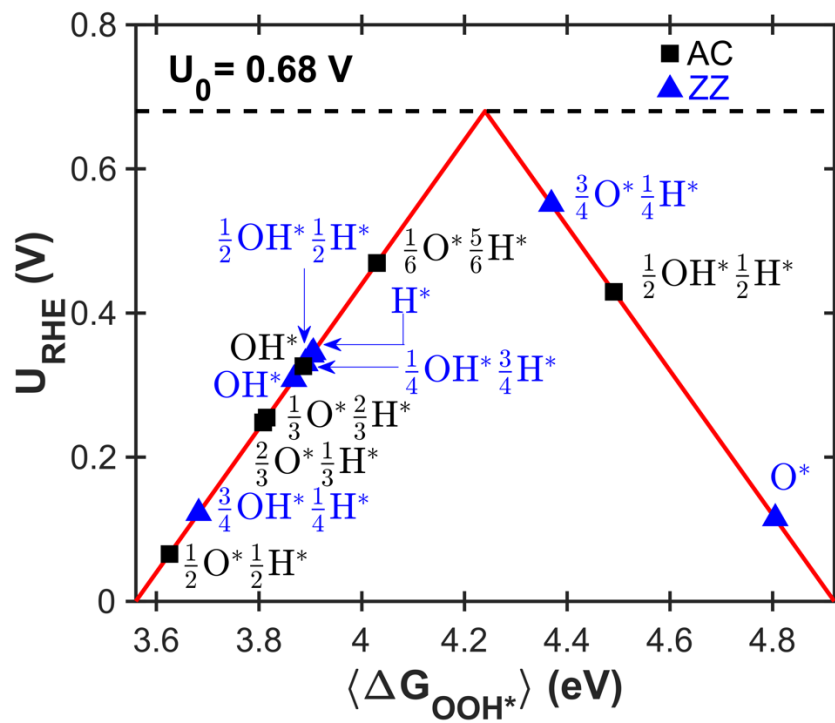


Figure S15. Theoretical activity volcano for 2-electron ORR at graphene edge sites. Theoretical activity volcano for 2-electron oxygen reduction showing activity predictions of the most stable active sites on various edge site termination configurations.

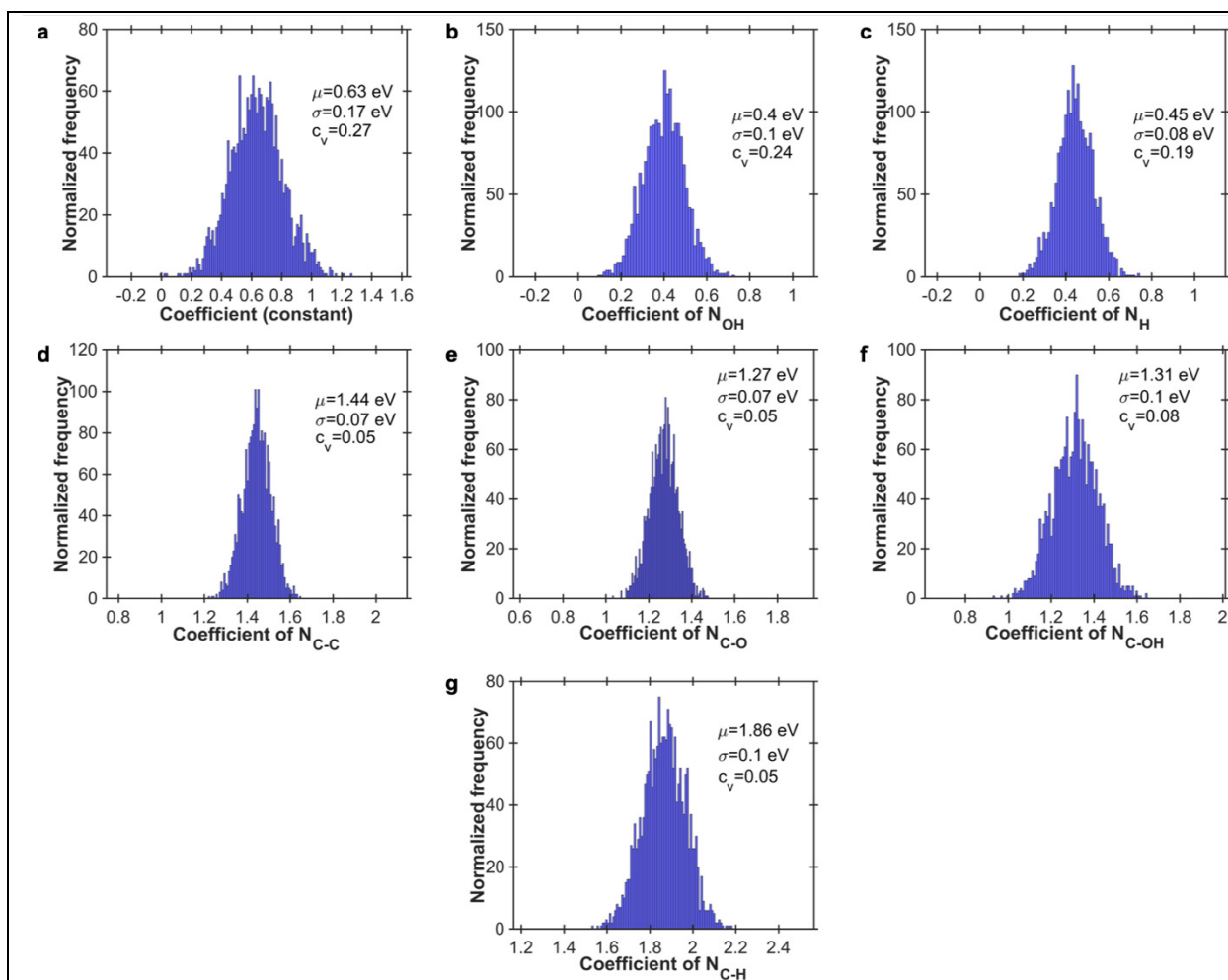


Figure S16. Distributions of coefficients in the structure-property relationship. Distributions obtained by constructing an ensemble of models using error estimation capabilities available within the BEEF-vdW exchange correlation functional. We observe tight distributions for the coefficients based on the coefficient of variation, which indicates robustness of the constructed structure-activity relationship.

Table S1. Data summary for Raman analysis for all NT-3DFG synthesis conditions ($n = 3$).								
Sample	$I_D I_G^{-1}$	$I_{2D} I_G^{-1}$	Position_D (cm⁻¹)	Position_G (cm⁻¹)	Position_{2D} (cm⁻¹)	FWHM_D (cm⁻¹)	FWHM_G (cm⁻¹)	FWHM_{2D} (cm⁻¹)
700 °C 30 min	2.34 ± 0.52	0.51 ± 0.09	1335.6 ± 3.8	1567.6 ± 5.4	2671.6 ± 7.4	48.8 ± 1.8	40.8 ± 2.2	83.4 ± 5.2
900 °C 30 min	3.59 ± 0.15	0.42 ± 0.03	1338.2 ± 1.2	1577.4 ± 2.4	2675.6 ± 3.8	58.0 ± 1.0	47.2 ± 1.6	102.4 ± 4.6
1100 °C 30 min	2.79 ± 0.11	0.52 ± 0.03	1338.2 ± 0.8	1579.0 ± 1.6	2674.6 ± 1.6	57.8 ± 1.0	49.0 ± 1.4	99.0 ± 4.0
1100 °C 60 min	2.36 ± 0.43	0.62 ± 0.13	1333.4 ± 2.6	1572.0 ± 4.4	2669.4 ± 5.0	57.6 ± 2.6	60.6 ± 3.0	99.6 ± 5.6
1100 °C 120 min	2.53 ± 0.16	0.61 ± 0.06	1338.2 ± 1.2	1578.6 ± 1.8	2676.6 ± 2.6	57.2 ± 1.4	57.6 ± 1.8	98.8 ± 5.0

Table S2. Data summary for Dual-laser Raman analysis of NT-3DFG synthesized at 700 °C for 30 min.				
Sample	Region	$I_D I_G^{-1}$	$FWHM_G$ (cm^{-1})	$Disp_G$ ($cm^{-1} nm^{-1}$)
1	1	2.46	34.2	0.12
	2	1.86	39.2	0.02
	3	2.11	37.8	0.02
	4	1.97	39.8	0.01
	5	2.73	39.6	0.03
	6	2.22	40.6	0.01
	7	1.95	40.2	0.02
	8	2.80	41.8	0.07
	9	2.43	39.6	0.02
	10	2.18	39.8	0.03
2	1	2.19	42.6	0.04
	2	2.55	42.4	0.03
	3	2.66	41.0	0.00
	4	2.89	43.4	0.00
	5	2.32	38.4	0.06
	6	2.00	41.4	0.03
	7	2.30	42.6	0.00
	8	2.21	42.0	0.00
	9	2.63	42.0	0.08
	10	2.70	43.6	0.05
3	1	2.16	39.6	0.03
	2	2.56	43.0	0.03
	3	1.96	39.6	0.01
	4	2.77	42.4	0.05
	5	2.05	41.2	0.06
	6	2.75	42.0	0.06
	7	2.19	40.4	0.02
	8	2.27	40.6	0.02
	9	2.24	38.8	0.00
	10	2.06	41.0	0.02

Table S3. Data summary for Dual-laser Raman analysis of NT-3DFG synthesized at 900 °C for 30 min.				
Sample	Region	$I_D I_G^{-1}$	$FWHM_G$ (cm^{-1})	$Disp_G$ ($cm^{-1} nm^{-1}$)
1	1	3.54	47.4	0.04
	2	3.63	46.8	0.08
	3	3.49	45.8	0.10
	4	3.49	47.8	0.05
	5	3.59	46.2	0.08
	6	3.56	47.4	0.07
	7	3.74	47.0	0.12
	8	3.57	46.2	0.05
	9	3.65	47.0	0.07
	10	3.51	46.4	0.04
2	1	3.54	46.0	0.04
	2	3.67	46.2	0.01
	3	3.72	48.0	0.06
	4	3.72	48.2	0.05
	5	3.59	47.8	0.06
	6	3.63	46.8	0.05
	7	3.51	46.8	0.06
	8	3.67	47.4	0.07
	9	3.55	47.0	0.05
	10	3.53	47.0	0.02
3	1	3.53	46.8	0.07
	2	3.44	48.8	0.00
	3	3.54	47.6	0.05
	4	3.71	47.0	0.11
	5	3.65	49.2	0.02
	6	3.53	48.8	0.18
	7	3.66	48.8	0.02
	8	3.54	47.0	0.09
	9	3.45	44.8	0.08
	10	3.73	48.4	0.14

Table S4. Data summary for Dual-laser Raman analysis of NT-3DFG synthesized at 1100 °C for 30 min.				
Sample	Region	$I_D I_G^{-1}$	$FWHM_G$ (cm^{-1})	$Disp_G$ ($cm^{-1} nm^{-1}$)
1	1	2.90	48.4	0.07
	2	2.86	48.2	0.05
	3	2.78	48.4	0.04
	4	2.82	48.8	0.05
	5	2.77	49.4	0.06
	6	2.91	48.6	0.03
	7	2.89	49.6	0.05
	8	2.90	47.6	0.04
	9	2.97	48.4	0.06
	10	2.86	49.4	0.04
2	1	2.81	48.8	0.07
	2	2.91	48.6	0.04
	3	2.91	50.2	0.08
	4	2.93	49.8	0.02
	5	2.83	50.0	0.09
	6	2.90	48.6	0.03
	7	2.73	46.8	0.07
	8	2.85	48.4	0.04
	9	2.87	48.4	0.06
	10	2.80	48.8	0.04
3	1	2.62	49.4	0.08
	2	2.66	50.0	0.11
	3	2.66	49.8	0.08
	4	2.64	49.6	0.05
	5	2.78	49.8	0.07
	6	2.67	49.4	0.05
	7	2.75	49.2	0.06
	8	2.61	50.8	0.03
	9	2.65	49.6	0.05
	10	2.60	48.6	0.06

Table S5. Data summary for Dual-laser Raman analysis of NT-3DFG synthesized at 1100 °C for 60 min.				
Sample	Region	$I_D I_G^{-1}$	$FWHM_G$ (cm^{-1})	$Disp_G$ ($cm^{-1} nm^{-1}$)
1	1	3.16	55.6	0.01
	2	2.75	57.2	0.03
	3	2.65	55.2	0.00
	4	2.99	55.6	0.01
	5	2.83	54.4	0.03
	6	2.75	54.4	0.03
	7	2.77	55.6	0.01
	8	2.73	55.0	0.03
	9	2.83	58.6	0.01
	10	2.72	54.8	0.02
2	1	2.17	61.6	0.00
	2	2.10	65.0	0.02
	3	2.07	62.8	0.01
	4	1.77	62.4	0.00
	5	1.88	63.4	0.06
	6	2.20	60.0	0.00
	7	2.03	59.6	0.03
	8	2.08	63.6	0.02
	9	2.14	61.0	0.01
	10	2.10	60.8	0.01
3	1	1.92	65.2	0.04
	2	2.15	64.6	0.05
	3	3.15	68.8	0.02
	4	1.97	62.4	0.03
	5	2.56	65.8	0.06
	6	1.86	62.8	0.00
	7	2.17	60.8	0.02
	8	2.05	64.8	0.07
	9	2.15	65.0	0.08
	10	2.08	63.6	0.00

Table S6. Data summary for Dual-laser Raman analysis of NT-3DFG synthesized at 1100 °C for 120 min.				
Sample	Region	$I_D I_G^{-1}$	$FWHM_G$ (cm^{-1})	$Disp_G$ ($cm^{-1} nm^{-1}$)
1	1	2.23	62.2	0.08
	2	2.37	64.8	0.09
	3	2.38	66.0	0.10
	4	2.04	63.6	0.07
	5	2.15	61.2	0.08
	6	2.20	63.4	0.05
	7	2.21	62.8	0.05
	8	2.38	64.6	0.08
	9	2.44	65.2	0.02
	10	2.18	64.8	0.10
2	1	2.57	55.6	0.04
	2	2.47	54.2	0.03
	3	2.54	55.2	0.02
	4	2.58	57.4	0.01
	5	2.35	55.2	0.00
	6	2.38	54.2	0.04
	7	2.50	55.4	0.01
	8	2.58	56.0	0.01
	9	2.65	55.4	0.04
	10	2.47	55.2	0.00
3	1	2.78	54.2	0.06
	2	2.81	52.6	0.05
	3	2.82	52.6	0.03
	4	2.82	53.4	0.03
	5	2.80	53.6	0.04
	6	2.85	53.4	0.03
	7	2.86	52.6	0.03
	8	2.81	53.2	0.03
	9	2.93	54.0	0.03
	10	2.81	51.8	0.02

Table S7. Data Summary for H₂O₂ Selectivity of NT-3DFG.			
Sample:	<i>n</i> = 1	<i>n</i> = 2	<i>n</i> = 3
Total integrated charge (C):	-2.12	-1.72	-2.29
Electrons consumed ($\mu\text{mol e}^-$):	22.0	17.8	23.7
Measured H ₂ O ₂ generated ($\mu\text{mol H}_2\text{O}_2$):	10.1	8.6	10.6
e ⁻ /H ₂ O ₂ Ratio:	2.18	2.07	2.24
Overall e ⁻ /H ₂ O ₂ ratio:	2.16 ± 0.09		
Overall H ₂ O ₂ Selectivity:	93 ± 3 %		

Table S8. Data summary for Raman analysis for NT-3DFG before & after ORR.								
Sample	I _D I _G ⁻¹	I _{2D} I _G ⁻¹	Position _D (cm ⁻¹)	Position _G (cm ⁻¹)	Position _{2D} (cm ⁻¹)	FWHM _D (cm ⁻¹)	FWHM _G (cm ⁻¹)	FWHM _{2D} (cm ⁻¹)
Pristine	2.83 ± 0.04	0.53 ± 0.04	1335.8 ± 0.6	1578.4 ± 0.8	2674.4 ± 1.2	55.0 ± 0.8	53.2 ± 0.8	98.6 ± 2.2
Post-ORR	2.84 ± 0.13	0.48 ± 0.04	1338.6 ± 0.8	1574.2 ± 1.8	2679.6 ± 2.2	60.6 ± 0.6	60.0 ± 1.8	102.4 ± 1.4

Table S9. Data summary for XPS analysis of NT-3DFG before & after ORR. ORR testing included cyclic voltammetry and H₂O₂ selectivity.					
Condition	Sample	Peak	Peak BE (eV)	Peak FWHM (eV)	Composition (at %)
Pristine	<i>n</i> = 1	C1s	284.9	3.1	99.6
		O1s	532.9	-	trace (< 1)
	<i>n</i> = 2	C1s	285.1	3.4	99.1
		O1s	533.2	-	trace (< 1)
	<i>n</i> = 3	C1s	284.9	3.2	99.8
		O1s	531.7	-	trace (< 1)
	average	C1s	285.0 ± 0.1	3.2 ± 0.1	99.5 ± 0.4
		O1s	532.6 ± 0.8	-	-
Post ORR	<i>n</i> = 1	C1s	284.9	3.5	86.1
		O1s	533.1	3.2	13.2
		Si2s	153.5	-	trace (< 1)
	<i>n</i> = 2	C1s	284.7	2.6	87.6
		O1s	532.6	3.4	10.7
		Si2s	153.1	3.7	1.7
	<i>n</i> = 3	C1s	284.7	2.7	88.6
		O1s	532.6	3.6	10.5
		Si2s	152.6	-	trace (< 1)
		N1s	399.6	-	trace (< 1)
	average	C1s	284.8 ± 0.1	2.9 ± 0.5	87.4 ± 1.2
		O1s	532.8 ± 0.3	3.4 ± 0.2	11.5 ± 1.5
Si2s		153.1 ± 0.5	-	-	

Table S10. Data summary for C1s & O1s chemical states of NT-3DFG after ORR. ORR testing included cyclic voltammetry and H₂O₂ selectivity.

Peak	Sample	State	Peak BE (eV)	FWHM (eV)	Ratio
C1s	<i>n</i> = 1	C-C	284.3	1.3	1.00
		C-OH	286.0	1.5	0.05
		C=O	287.0	1.5	0.02
		O=C-OH	288.5	1.5	0.03
		Plasmon	290.6	2.0	0.02
	<i>n</i> = 2	C-C	284.1	1.2	1.00
		C-OH	285.9	1.4	0.11
		C=O	286.9	1.4	0.06
		O=C-OH	288.1	1.4	0.03
		Plasmon	290.5	3.7	0.09
	<i>n</i> = 3	C-C	283.9	1.1	1.00
		C-OH	285.2	1.3	0.09
		C=O	286.4	1.3	0.03
		O=C-OH	287.7	1.3	0.03
		Plasmon	290.2	3.0	0.06
	average	C-C	284.1 ± 0.2	1.2 ± 0.1	1.00
		C-OH	285.7 ± 0.4	1.4 ± 0.1	0.08 ± 0.03
		C=O	286.8 ± 0.3	1.4 ± 0.1	0.04 ± 0.02
		O=C-OH	288.1 ± 0.4	1.4 ± 0.1	0.03 ± 0.01
		Plasmon	290.4 ± 0.2	2.9 ± 0.1	0.06 ± 0.04
O1s	<i>n</i> = 1	C-OH	532.1	1.6	1.00
		C=O	533.3	1.6	0.70
		O=C-OH	531.0	1.6	0.41
	<i>n</i> = 2	C-OH	532.0	1.6	1.00
		C=O	533.2	1.6	0.65
		O=C-OH	530.9	1.6	0.34
	<i>n</i> = 3	C-OH	532.4	1.4	1.00
		C=O	533.2	1.4	0.71
		O=C-OH	531.3	1.4	0.25
	average	C-OH	532.2 ± 0.2	1.5 ± 0.1	1.00
C=O		533.2 ± 0.1	1.5 ± 0.1	0.69 ± 0.03	
O=C-OH		531.1 ± 0.2	1.5 ± 0.1	0.33 ± 0.08	

Table S11. Data summary for explored ZZ and AC active sites including local coordination environment.

Active Site		ΔG_{OOH}	N_O	N_{OH}	N_H	N_C	N_{C-O}	N_{C-OH}	N_{C-H}
ZZ	H*	3.914	0	0	1	2	0	0	0
	H* (basal)	5.308	0	0	0	3	0	0	0
	H*	3.905	0	0	1	2	0	0	0
	3/4O*1/4H*	4.369	0	0	0	1	2	0	0
	O*	4.805	0	0	0	1	2	0	0
	1/4OH*3/4H*	3.890	0	1	0	2	0	0	0
	OH*	3.868	0	1	0	2	0	0	0
	1/4O*3/4H*	5.411	0	0	1	3	0	0	0
	3/4O*1/4H*	4.663	0	0	0	1	2	0	0
	1/4O*3/4H*	5.342	0	0	0	1	1	0	1
	1/2O*1/2H*	5.252	0	0	0	1	1	0	1
	3/4O*1/4H*	4.369	0	0	0	1	2	0	0
	1/2OH*1/2H*	3.902	0	1	0	2	0	0	0
	1/2OH*1/2H*	4.935	0	0	0	1	0	1	1
3/4OH*1/4H*	3.893	0	1	0	2	0	0	0	

	3/4OH*1/4H*	3.811	0	1	0	2	0	0	0
	3/4OH*1/4H*	3.682	0	0	1	2	0	0	0
	OH*	4.812	0	0	0	1	0	2	0
AC	1/6O*5/6H*	4.029	0	0	1	1	1	0	0
	1/3O*2/3H*	3.815	0	0	1	1	1	0	0
	1/2O*1/2H*	3.626	0	0	1	1	1	0	0
	2/3O*1/3H*	3.808	0	0	1	1	1	0	0
	OH*	3.886	0	1	0	1	0	1	0
	1/3O*2/3H*	4.633	0	0	0	2	1	0	0
	1/3O*2/3H*	3.975	0	0	1	1	1	0	0
	1/2O*1/2H*	3.644	0	0	1	1	1	0	0
	1/6O*5/6H*	4.906	0	0	0	2	1	0	0
	1/6O*5/6H*	4.048	0	0	1	1	1	0	0
	1/2OH*1/2H*	4.491	0	1	0	1	0	0	1